

Skoltech

Skolkovo Institute of Science and Technology

Skolkovo Institute of Science and Technology

SINGLE-WALLED CARBON NANOTUBES AS A SOURCE OF ULTRASOUND

Doctoral Thesis

by

STEPAN ROMANOV

DOCTORAL PROGRAM IN PHYSICS

Supervisor

Professor Dr. Sci. Albert Nasibulin

Moscow - 2020

(© Stepan Romanov 2020)

I hereby declare that the work presented in this thesis was carried out by myself at Skolkovo Institute of Science and Technology, Moscow, except where due acknowledgement is made, and has not been submitted for any other degree.

Candidate (Stepan Romanov)

Supervisor (Prof. Albert Nasibulin)

Abstract

Single-walled carbon nanotubes (SWCNTs) being a unique nanomaterial demonstrate outstanding performance in mechanical, optical, electrical, and other applications. The superior physical properties of SWCNTs along with fast, scalable, and inexpensive production make them promising material for the implementation in devices of the future.

Thermophone is a sound-producing device exploiting thermoacoustic effect, which performance significantly depends on the heat capacity per unit area (HCPUA) of the utilized material. Recent observations reveal enhanced performance of thermophones based on novel nanomaterials owing to low HCPUA. However, further development of thermophones requires sophistication of theoretical models, introduction of new technological approaches, and additional advances in materials.

This thesis addresses important theoretical and experimental aspects of thermophones. The comprehensive experimental investigation carried out with SWCNT films as the main element of a thermophone. The theoretical approaches extended here to obtain an analytic formula for the sound pressure in the ultrasound region using diffraction corrections. Theoretical derivations are confirmed by experiments and numerical simulations. For the audio region, thermophones efficiency is close to the theoretical ultimate limit, whereas in the ultrasound region the efficiency is suppressed by the heat accumulation effect in thermophones. The work demonstrates a few methods to enhance the thermophones performance: 1) pulse induced sound generation; 2) SWCNT films protection from the influence of an environment; 3) SWCNTs purification from catalyst residuals. The first method leads to increase of the sound pressure owing to overcome the heat accumulation problem and applies to thermophones based on any material. Methods 2 and 3, in turn, significantly increase the performance of thermophones based on carbon nanotubes in terms of sound pressure and protection from harsh environment.

A special accent in the work was made on method 3, because it introduces a technique with a huge potential for further implementation in the field of CNTs. The

technic represents a method for the rapid purification of SWCNT films from catalyst impurities by Joule heating in a vacuum allowing to decrease the catalyst concentration by a factor of 27 (from 17 to <1 wt.%) after heating at 1600 °C for 2 min. The Joule-assisted purification leads to an increase of the sound pressure in thermophones due to smaller heat capacity of purified films. The results are extendable to a number of other applications, for instance, bolometric detectors.

Overall, to the best of our knowledge, the research demonstrates the highest sound pressure of 101 dB (at 100 kHz, 3 cm distance and 1 W of input power) for thermophones made of SWCNT film in ultrasound region compared to all published materials for thermophone application, due to uniqueness of the SWCNT films. The promising results allow to utilize thermophones based on SWCNT films for such applications as calibration of ultrasound equipment or as antennas for robots positioning.

Publications

1. **Romanov, S.A.**, Aliev, A.E., Fine, B.V., Anisimov, A.S., and Nasibulin, A.G. Highly efficient thermophones based on freestanding single-walled carbon nanotube films. *Nanoscale Horizons*, 4(5), 1158-1163, (2019).
2. **Romanov, S.A.**, Alekseeva A.A., Khabushev E.M., Krasnikov D.V., and Nasibulin A.G., Rapid, efficient, and non-destructive purification of single-walled carbon nanotube films from metallic impurities by Joule heating. *Carbon*, 168, 193-200 (2020).
3. Aliev, A.E., Codoluto, D., Baughman, R.H., Ovalle-Robles, R., Inoue, K., **Romanov, S.A.**, Nasibulin, A.G., Kumar, P., Priya, S., Mayo, N.K. and Blottman, J.B., Thermoacoustic sound projector: exceeding the fundamental efficiency of carbon nanotubes. *Nanotechnology*, 29(32), 325704, (2018).

Author's Contribution

Publication 1: Highly efficient thermophones based on freestanding single-walled carbon nanotube films.

The author is mainly responsible for this work. The author assembled and automatized setup, designed & conducted the experiments, arranged numerical modelling, participated in theory derivation and analysed the data. The author was responsible for writing the manuscript, communicating with the journal editor and answering to the reviewers' queries.

Publication 2: Rapid, efficient, and non-destructive purification of single-walled carbon nanotube films from metallic impurities by Joule heating.

The author is mainly responsible for this work. The author assembled and automatized setup, designed & conducted the experiments, analysed the data, arranged numerical modelling and theoretical interpretation. The author was responsible for writing the manuscript, communicating with the journal editor and answering to the reviewers' queries.

Publication 3: Thermoacoustic sound projector: exceeding the fundamental efficiency of carbon nanotubes.

The author participated in experiments, contributed to the interpretation of the experimental results and writing the manuscript.

Other featured publications

1. Gilshteyn, E. P., **Romanov, S. A.**, Kopylova, D. S., Savostyanov, G. V., Anisimov, A. S., Glukhova, O. E., and Nasibulin, A. G. Mechanically Tunable Single-Walled Carbon Nanotube Films as a Universal Material for Transparent and Stretchable Electronics. *ACS Applied Materials & Interfaces*, 11(30), 27327-27334, (2019).

2. Tsapenko, A. P., **Romanov, S. A.**, Satco, D. A., Krasnikov, D. V., Rajanna, P. M., Danilson, M., and Nasibulin, A. G. Aerosol-assisted fine-tuning of optoelectrical properties of SWCNT films. *The Journal of Physical Chemistry Letters*, 10(14), 3961-3965, (2019).

4. Krasnikov, D.V., Zabelich, B.Y., Iakovlev, V.Y., Tsapenko, A.P., **Romanov, S.A.**, Alekseeva, A.A., Grebenko, A.K. and Nasibulin, A.G., A spark discharge generator for scalable aerosol CVD synthesis of single-walled carbon nanotubes with tailored characteristics. *Chemical Engineering Journal*, 372, 462-470, (2019).

3. Lashkov, A.V., Fedorov, F.S., Vasilkov, M.Y., Kochetkov, A.V., Belyaev, I.V., Plugin, I.A., Varezchnikov, A.S., Filipenko, A.N., **Romanov, S.A.**, Nasibulin, A.G. and Korotcenkov, G., The Ti wire functionalized with inherent TiO₂ nanotubes by anodization as one-electrode gas sensor: A proof-of-concept study. *Sensors and Actuators B: Chemical*, 306, 127615, (2020).

Acknowledgements

I would like to thank all the people who were surround me for these years of my PhD. I believe that even indirect participation influenced my work and made it what it is. Personally, I want to thank my scientific supervisor and head of the Laboratory of Nanomaterials (LNM) Prof. Albert Nasibulin for guidelines, opportunities, and patience during my PhD work. It was a great experience to work with you and participate in a building of a scientific laboratory from a scratch, starting from 2014 when I joined LNM as a MS student and then from 2016 to 2020 as a PhD student. For these periods a rapid development took place in Skoltech in general and in LNM, in particular. I hope even more improvements are expecting us in the future.

My perception of the role of experiments in scientific work was highly influenced by Prof. Ali Aliev, who significantly helped me on my initial steps in the thermoacoustic field. For those times, when we in Skoltech did not have equipment, Prof. Ali Aliev kindly hosted me in the University of Texas at Dallas and shared the facilities of NanoTech Institute. Also, Prof. Ali Aliev should get the main credits for the work on Thermoacoustic sound projector: exceeding the fundamental efficiency of carbon nanotubes, where I was happy to participate and contribute to experiments and results interpretation. Also, I want to highlight the role of Prof. Boris Fine, who helped me a lot with theoretical investigation of thermophone.

I want to thank all the past and present members of LNM and especially Evgenia Gilshteyn and Alena Alekseeva.

Table of Contents

Abstract	3
Publications	5
Acknowledgements	8
Abbreviations	11
Chapter 1. Introduction.....	12
Chapter 2. The thermoacoustic effect and introduction to thermophones.....	15
2.1 Sound and its applications.....	15
2.2 Origin of thermoacoustic effect.....	16
2.3 Thermophones	17
Chapter 3. Methods and characterization	20
3.1 Synthesis of SWCNTs.....	20
3.2 Characterization of SWCNT films.....	22
3.2.1 SEM and TEM.....	22
3.2.2 Raman spectroscopy	24
3.2.3 UV-vis-NIR spectroscopy	27
3.2.4 Fourier-transform infrared spectroscopy	28
3.3 Sound measurements.....	29
3.4 Temperature measurements.....	31
Chapter 4. Results and discussions.....	34
4.1 Theory of thermophones	34

4.1.1	Temperature oscillations.....	35
4.1.2	Density and velocity oscillations near the sample surface	39
4.1.3	Pressure oscillations near the sample surface	40
4.1.4	Flat transducers and intensity gain	42
4.1.5	Volumetric heaters.....	46
4.1.6	Numerical model of thermophone.....	50
4.2	Temperature control of SWCNT films: theory and experiment	52
4.2.1	Energy dissipated by convection effect	53
4.2.2	Energy dissipated by thermal conductivity	57
4.2.3	Energy dissipated from SWCNT film by the radiation effect	58
4.3	Highly efficient thermophones based on SWCNT films	60
4.3.1	Amplitude frequency response of SWCNT based thermophones	60
4.3.2	Acoustic field anisotropy and diffraction correction.....	67
4.4	Increasing the performance of SWCNT films.....	70
4.4.1	Joule assisted purification and its effect on thermophones efficiency	71
4.4.2	Environment protected thermophones.....	81
4.4.3	Pulse induced sound generation	84
4.5	Application of thermophones.....	88
	Chapter 5. Conclusions.....	92
	Bibliography.....	94
	Appendix: List of variables	106

Abbreviations

AC alternating current

CNT carbon nanotube

CVD chemical vapor deposition

DC direct current

ITO indium tin oxide

FTIR Fourier-transform infrared spectroscopy

GMRES generalized minimal residual

HCPUA heat capacity per unit area

MWCNT multiwalled carbon nanotube

PARDISO parallel direct sparse solver

PEDOT:PSS polystyrene sulfonate

UV-vis-NIR ultraviolet-visible-near infrared spectroscopy

RBM radial breathing mode

SEM scanning electron microscopy

SWCNT single-walled carbon nanotube

TEM transmission electron microscopy

2D two dimensional

3D three dimensional

Chapter 1. Introduction

Sound provides unprecedented opportunities to simplify and improve our lives. Ultrasound, in particular, is widely applicable in healthcare^{1,2}, industry^{3,4} and technology^{5,6}. Among the ultrasound producing devices there are many, exploiting thermoacoustic effects. For instance, photoacoustic effect, where laser heating of substance leads to sound propagation⁷. Photoacoustic based devices apply in non-destructive imaging⁸, tumor treatments⁹ and other applications¹⁰. This thesis addresses a thermophone, which is the thermoacoustic device, where sound propagation arises from the Joule heating of a substance under an impact of alternating current. Principal limitation of sound pressure in thermophones is large heat capacity per unit area (HCPUA) of utilized materials.

Recent advances in materials science and technology have sparked a new wave of research on thermophones¹¹. Novel nanomaterials became thinner and sparser. Hence, they had lower HCPUA, which resulted in a significant increase in the sound pressure and made thermophones attractive for many applications. Promising results for air-coupled thermophones based on different nanostructured conducting materials were observed in many materials such as: gold nanowires¹², poly(3,4ethylenedioxythiophene) polystyrene sulfonate (PEDOT:PSS)¹³, silver nanowires¹⁴, indium tin oxide (ITO)¹⁵, thin titanium film¹⁶, graphene¹⁷, multiwalled carbon nanotubes (MWCNTs)¹⁸ and thin aluminum wires¹⁹. Up to the present moment, the best performance in the thermophones was demonstrated by carbon allotropes.

Tremendous interest to carbon nanotubes (CNTs), in general, and single-walled carbon nanotubes (SWCNTs), in particular, was initiated by works of Iijima^{20,21}. Theoretically predicted and experimentally measured outstanding properties of this material made it one of the most perspective material towards applications in the last decades²². SWCNTs demonstrate fascinating structural, mechanical, and optoelectrical properties, which inspire a vast number of applications in catalysis, electronics, photonics, medicine, photovoltaics *etc.*^{23,24,25,26}. The outstanding properties of SWCNTs make them a perspective candidate for the applications in thermophones.

Overall, the field of thermophone is modern and requires new materials and methods towards an increase of its efficiency. In this work, the comprehensive study of thermophones, which cover theoretical and experimental aspects, was carried out. For the first time, a comprehensive research was performed using SWCNT films synthesized by the floating catalyst method. From a theoretical point of view, the focus of the research was made on analytical description of sound pressure dependency on the frequency in ultrasound region. From the experimental side, a few novel approaches to increase the thermophone efficiency were proposed. The work results demonstrate the highest sound pressure level of freestanding SWCNT films among other materials in thermophone.

This thesis is based on 3 publications and comprise from 5 chapters. Chapter 2 introduces a history of thermoacoustic effect and thermophones. Chapter 3 includes the description of experimental approaches and methods used in the thesis research. Chapter 4

presents the main findings of this work including theoretical and experimental investigations. Chapter 5 summarizes the main work results.

Chapter 2. The thermoacoustic effect and introduction to thermophones

2.1 Sound and its applications

Sound is defined as oscillation in pressure, stress, particle displacement, particle velocity, etc., propagated in a medium with internal forces (*e.g.*, elastic or viscous), or as the superposition of such propagated oscillations²⁷. In terms of oscillation frequency (f), the sound bandwidth historically divided into three groups: infrasound (<20 Hz), audio (20 Hz – 20kHz) and ultrasound (>20kHz). The division appeared because human hears the frequencies in the range of 20 Hz – 20 kHz. Despite the inability of humans to hear ultrasound and infrasound they found many useful applications in medicine²⁸, industry²⁹, science^{30,31}, etc³².

Ultrasound due to the small wavelength ($\lambda = v_s / f$, where v_s is the speed of sound) find important applications in imaging^{33,34}, cleaning³⁵, mixing³⁶, destructing³⁷, and other fields³⁸. Ultrasound devices utilize the effect of cavitation and properties of ultrasound as a wave, in particular: reflection, transmission, focusing, *etc.* The cavitation leads to a high level of disturbance in the media and applicable for cleaning, mixing, and destructing needs. On the one hand, the wave properties of sound allow utilizing ultrasound in non-destructive imaging applications using reflection and transmission schemes³⁹. On the other hand, ultrasound focusing reveals enough power to destruct tumors⁴⁰ or weld materials⁴¹.

Infrasound is of utmost importance for our health and plays a significant role in nature. Infrasound has a large wavelength, which influences humans by resonances with

the body and cause harm⁴². Also, many nature phenomena such as earthquake⁴³, volcano eruption^{32,44} accompanied by infrasound waves. Low infrasound attenuation leads to signal propagation to thousands of kilometers⁴⁵ and the detection of such waves can warn and prevent disasters. Moreover, infrasound plays an important role in atmospheric processes including monitoring of thunderstorms^{46,47} and nuclear-explosion tests⁴⁸.

Significant role of sound equipment in our daily life requires constant development of sound generators and detectors. Usually, the sound is created by periodic mechanical vibrations of rigid or semi-rigid objects, which cause pressure oscillations in a medium and result in sound propagation. However, an alternative mechanism of sound generation without mechanical vibrations of the material itself exists.

2.2 Origin of thermoacoustic effect

Thermoacoustic effect is a phenomenon in which thermal energy transforms into sound and *vice versa*. The thermoacoustic generation is based on periodical thermal expansions of heated material or surrounding media. The first mention of thermoacoustic effect in history is a subject of debates, however, we can agree that the Rijke tube is the simplest thermoacoustic sound generating device⁴⁹. The device construction requires only hollow tube and flame. Heating the air inside the tube from one side produces sound. The sound in the Rijke tube has a resonance nature, defined by tube geometry, and produces single frequency with its harmonics.

The thermoacoustic effect finds applications in the real-life system being a part of engines⁵⁰, gas separators⁵¹, heat pumps⁵², refrigerators^{53,54}, and other devices⁵⁵. Scientists

found thermoacoustic based devices less damaging to the environment and not causing the greenhouse effect^{56,57}. The majority of the thermoacoustic devices exploit the photoacoustic effect, in which the thermal energy is applied by periodic electromagnetic radiation. Experimentally, the photoacoustic effect was observed in 1859 by Alexander Graham Bell, who called the operating device nonelectric photophone⁵⁸. Unlike the Rijke tube, the photophone generates the sound of any frequencies which leads to a wide bandwidth of such sound sources. For the photophone, the frequency of sound matches with the frequency of radiation modulation. Currently, photo-acoustics employs in a diverse range of applications, including gas detection in pollution monitoring⁵⁹, biomedical applications⁶⁰, and in the analysis of material properties⁶¹.

2.3 Thermophones

This thesis covers a type of thermoacoustic device which exploits alternating Joule heating to produce the sound. The device is called thermophone and potentially any conducting material under resistive heating can be utilized as thermophone. The first thermophones, experimentally obtained in 19th century, were based on the metallic films⁶². In 1917, Arnold and Crandall⁶³ theoretically explained the thermal origin of sound in thermophones. According to their theory, alternating current causes Joule heating, which leads to temperature oscillations in a conductor, which, in turn, leads to periodic thermal expansion of the surrounding gas and, as a result, generate sound. The principal relation of the theory was $p \sim \sqrt{f}/C_s$, where p is the sound pressure and $C_s = \rho_a C_h$ is the heat capacity per unit area (HCPUA). The latter is defined as the product of the heat capacity of material

per unit mass, C_h , and the areal density of the sample, $\rho_a = h\rho_h$, where h is the thickness of the sample and ρ_h is its density. Thermophone and photophone both have wide bandwidth, however, in case of photophone, frequencies of sound and light modulation are the same, while for thermophone, frequency of sound is doubled frequency of current modulation. The convenient sound generation with the alternating current along with frequency doubling are main thermophones advantages attractive for the ultrasound applications. However, the first thermophones had low sound pressure and low efficiency, because they were based on metallic films having a large thickness and high density, which means high HCPUA.

Advances in material science lead to an increase of thermophones performance due to HCPUA¹¹ lowering. Moreover, experimental investigations of the materials having a small HCPUA shed light on the theory of thermophones. The gas heat capacity of air per unit mass, C_g , was observed to be a new limiting factor for achieving higher sound pressures. In 2008 Xiao *et al.*⁶⁴ introduced the relation for the sound pressure of materials with small HCPUA, $p \sim f/C_g$. Having said that the relation is frequency dependent, which mean the domination of C_s over heat properties of the media at ultrasound frequencies and switching from relation of Xiao to relation of Arnolds even for materials with ultralow HCPUA. This fact indicates an importance of further attempts in decreasing of HCPUA to enhance thermophones sound pressure at ultrasound frequencies. The main limitation of Arnolds and Xiao theories is the point-source approximation. It is not applicable, when wavelengths become comparable or smaller, than the size of the sample. The need to take

into account the finite size of thermophones at high frequencies has been already demonstrated numerically and experimentally by Vesterinen *et al.*¹⁹ Hence, the theory requires theoretical modifications to describe sound pressure of a finite and large sources at high frequencies.

Chapter 3. Methods and characterization

3.1 Synthesis of SWCNTs

A variety of methods for carbon nanotubes synthesis exists, such as: arc-discharge, laser ablation and others^{65,66}. Among all methods towards the CNTs synthesis, the aerosol floating catalyst chemical vapor deposition (CVD) method^{67,68} has many advantages such as: easy sample handling, large surface area of the samples, and convenient control of sample thickness during the synthesis process. Moreover, fast, scalable and inexpensive production of high-quality SWCNT films makes this synthesis method attractive for industrial applications such as: transparent capacitive touch sensors, thin-film transistors, electrochemical sensors, polymer-free saturable absorbers, bright organic light-emitting diodes, gas flowmeters, and gas heaters^{69,70}.

For this work, the SWCNTs were synthesized in a flow reactor by aerosol floating catalyst CVD method described in detail elsewhere^{69,71}. Briefly, ferrocene as a catalyst precursor was introduced in a hot zone (880°C) of a tubular quartz reactor in the atmosphere of carbon monoxide (Figure 3.1-1a). The Boudouard reaction ($2\text{CO} = \text{C} + \text{CO}_2$), which occurs on the surface of formed catalyst particles, resulted in the release of carbon and formation of SWCNTs. The SWCNTs were collected downstream of the reactor by the aerosol filtration in the form of randomly oriented nanotube film on a microporous nitrocellulose filters (0.45 μm , HAWP, Merck Millipore, USA). The surface area of the films may reach dozens of squared centimeters (Figure 3.1-1b). During the synthesis process, the SWCNT film thickness was managed by the collection time.

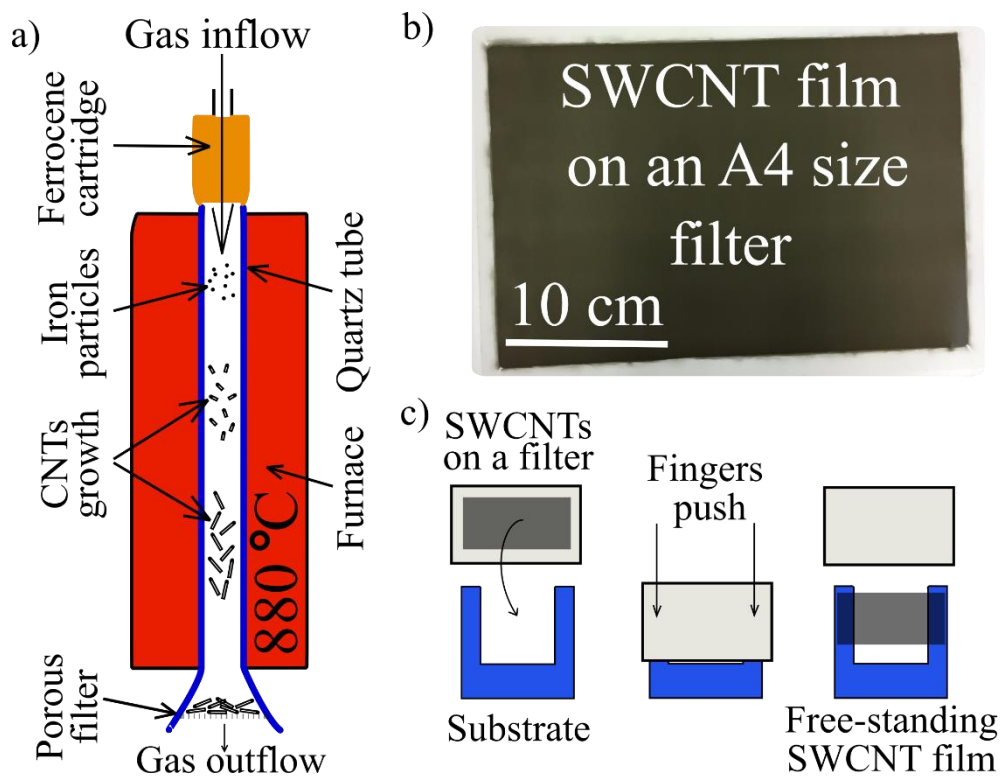


Figure 3.1-1. a) Schematic representation of the reactor for SWCNTs synthesis by floating catalyst method. b) SWCNTs on a filter with a large surface area of 21.0 x 29.7 cm². c) Schematic representation of free-standing SWCNT film fabrication.

The quality of the SWCNTs was controlled by Raman spectroscopy, ultraviolet-visible-near infrared (UV-vis-NIR) spectroscopy, scanning electron microscopy (SEM), transmission electron microscopy (TEM) methods described in detail in the following sections. An important advantage of the filter-based collection is the great flexibility of the further utilization of the produced SWCNT films. The films can be easily transferred from the filter onto various substrates and even in the freestanding form (Figure 3.1-1c) due to low adhesion of SWCNTs to filter⁷⁰.

3.2 Characterization of SWCNT films

3.2.1 SEM and TEM

Electron based microscopy is commonly used technique for materials characterization, that give insights into morphology, composition, processes on the nanoscale level, *etc.* Utilization of accelerated electrons for imaging purposes allows to reach a few orders higher resolution than that for the photon-based microscopes. To obtain a sub-nanometer resolution and internal structure of the material, the transmission electron microscopy (TEM) is used⁷². In TEM the electrons pass through the sample and are collected on a detector. In the simplest case, the brightness of the image pixel depends on the number of transmitted electrons⁷³. To perform TEM imaging sample thickness has to be on the scale of nanometers. For the purposes of morphology investigation of thick samples or on larger scales, the scanning electron microscopy (SEM) is utilized⁷⁴. The construction of SEM image is based on the secondary electrons emitted from the surface of the material under the impact of the incident beam of electrons⁷⁵. For SEM images the brightness of the pixel depends on the number of detected secondary electrons.

To obtain the structure of an individual SWCNT in this work, a FEI Tecnai G2 F20 transmission electron microscope was used. Mostly, SWCNT film sample consists of joint SWCNTs, which we call bundles, however single tubes with a diameter of 2.2 nm can be observed as well (Figure 3.2-1a). TEM imaging was utilized to measure diameter distribution of iron nanoparticles and SWCNT bundles. The SEM images were taken with

FEI Helios 660 DualBeam microscope. Typical images of free-standing SWCNTs films demonstrate the random orientation of SWCNT bundles in a film (Figure 3.2-1b).

Also, the thesis includes a study on *in situ* heating of SWCNT film in TEM. The heating was performed to investigate an iron nanoparticles evaporation process from the films. The commercially available chips supplied by DENSsolutions company were utilized for that purpose. In experiments, a maximum operating temperature of chips was 1100 °C (DENS-C-SH30-4M-FS-SM SD1932-W5 / Box 111). The comprehensive description of the chip operation can be found in ⁷⁶. Briefly, the chip consists of a heating spiral incorporated within the suspended SiN_x membrane. The Joule heating of the spiral is initiated by an impact of the current and increases the temperature of the membrane. The temperature is controlled in a closed-loop by known dependency of the spiral resistance on temperature. In other words, the temperature was set by current and adjusted by 4-probe measurements of the spiral resistance.

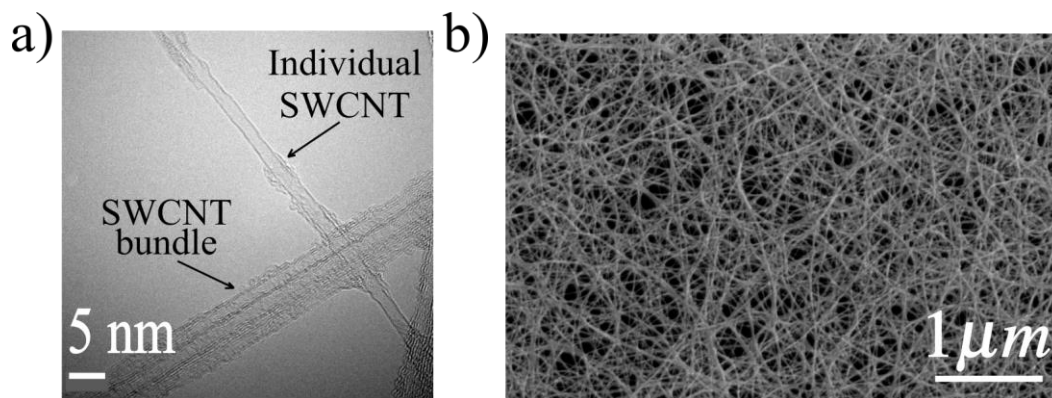


Figure 3.2-1. a) Image of an individual SWCNT taken in TEM. b) Typical image of SWCNT film morphology taken in SEM.

3.2.2 Raman spectroscopy

Raman spectroscopy is based on phonon scattering and allows to reveal vibrational modes of materials known as phonons⁷⁷. Only vibrations followed by a change in polarizability are active in Raman spectroscopy. The general idea of the spectroscopy is to illuminate material with a laser having photons frequency of ν_i and detect the scattered photons with a frequency ν_s . In fact, there are three important photon scattering processes: i) Rayleigh scattering, when the photon energy preserve in the process and $\nu_i = \nu_s$; ii) Stocks scattering, when $\nu_i > \nu_s$ with a phonon emitting; iii) Anti-Stocks scattering, when $\nu_i < \nu_s$ with a phonon absorbing (Figure 3.2-2a). Raman spectroscopy is based on ii) and iii) scattering processes. The difference in the photon frequencies $\nu_i - \nu_s$ (Raman shift) gives insights into vibrational modes of the material and usually is expressed in wavenumber units. Thus, the absolute values for Raman shift in Stocks and Anti-Stocks scattering are the same, however, the signal intensities are different. Stocks scattering process dominates for SWCNTs under ambient conditions.

Raman spectra of SWCNTs exhibit many peaks⁷⁸, here we discuss those of most importance: G, D, RBM, 2D (Figure 3.2-2b). Peaks position, shape, and intensity give insight into geometrical parameters, thermal properties, and electronic structure of carbon nanotubes. Radial breathing mode (RBM) corresponds to the vibration of a CNT in a radial direction. The existence of RBM peaks in Raman spectra is a benchmark arising only in CNTs at frequencies of 100-500 cm^{-1} . The position of RBM, as well as intensities, are defined by carbon nanotubes diameter and chirality^{79,80}. The G-band arises in nanotubes as

well as in other carbon sp^2 -hybridized materials and corresponds to optical phonons. For CNTs, G-band divides into two peaks G^+ and G^- unlike a single peak for graphite. The G^+ and G^- associate with longitudinal and transversal optical phonons and typically has a frequency of 1590 cm^{-1} and 1570 cm^{-1} , respectively. Both peak positions are sensitive to the diameter of nanotubes, whereas the G^+ position depends on the doping type and its level⁸¹. The D and 2D bands both arise from a double resonance process, which are typically utilized for defectiveness and temperature measurements⁷⁸. The ratio of G/D bands intensities characterize amount of defects in the sample, whereas 2D peak intensity exhibit strong dependence on the sample temperature.

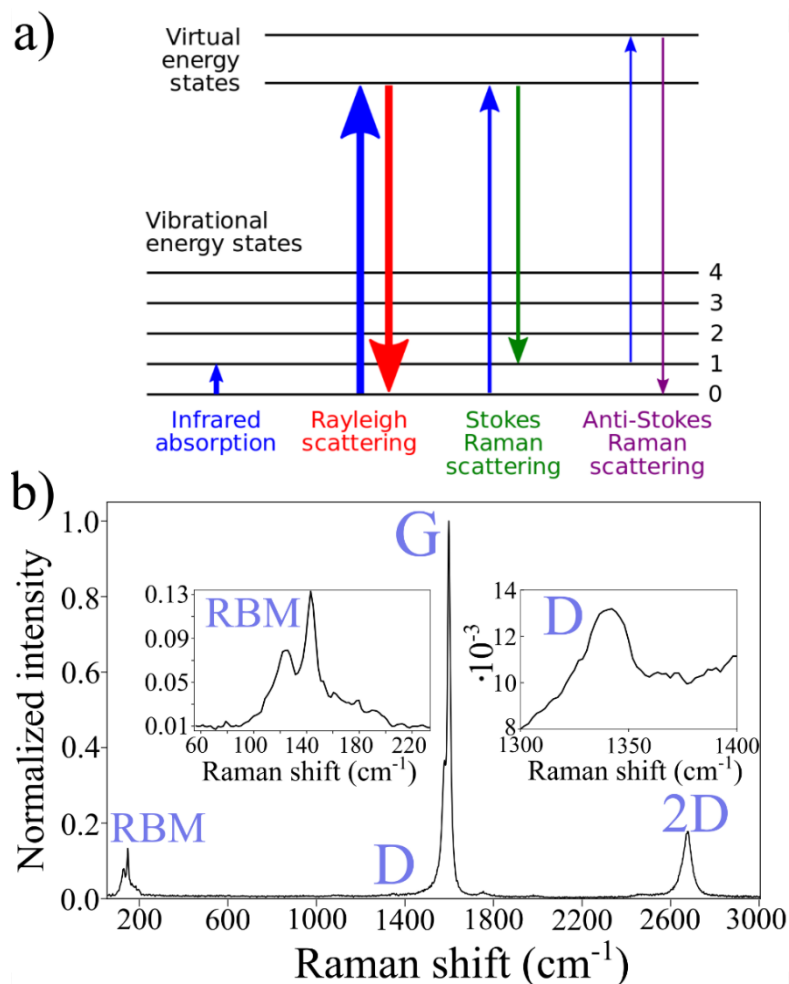


Figure 3.2-2. a) Energy-level diagram, showing the energy states involved in Raman spectroscopy. b) Typical Raman spectra of SWCNTs utilized in this thesis.

Raman spectra in this thesis were utilized to characterize the number of defects in the samples after Joule assisted purification in a vacuum. The measurements were performed using Thermo Scientific DXRxi Raman Imaging Microscope ($\lambda = 532$ nm, laser power of 0.1 mW).

3.2.3 UV-vis-NIR spectroscopy

The UV-vis-NIR spectroscopy is based on absorption or reflection of light from the matter in wavelengths ranging from ultraviolet to infrared region⁸². Only vibrational modes followed by a change in dipole moment are sensitive to absorption spectroscopy, for others, the Raman spectroscopy should be utilized. In general, spectroscopy is used to reveal the electronic structure and vibrational properties of the substance. Materials typically have unique spectra with an individual set of absorption peaks. Therefore, absorption spectroscopy defines the presence of certain compounds in the substance and defines its amount.

The absorption spectroscopy of SWCNTs includes a few important peaks: pi-plasmon, S₁₁, S₂₂, M₁₁. The pi-plasmon peak exhibits in all carbon allotropes and arises from pi electrons of carbon atoms. The S₁₁, S₂₂, M₁₁ absorption peaks arise from transitions between Van Hove singularities for semiconducting and metallic nanotubes⁷⁹ (Figure 3.2-3a). The peaks characterize whether the CNTs are metallic or semiconducting and are utilized to estimate its relative amount. The transmittance of CNT films in the visible range is of high importance for application in transparent conductive electronics. Therefore, scientists search for methods for modification of CNT films where an increase in conductivity would not accompany with changes in transmittance.

In this work, UV-vis-NIR spectroscopy was used to characterize the SWCNT films after Joule-assisted purification (Section 4.4.1). The optical spectra (Figure 3.2-3b) of SWCNT films of different thicknesses were measured using dual-beam spectrometer

Perkin Elmer Lambda 1050 (300 – 3000 nm; resolution of 2 nm). The S_{11} , S_{22} , and M_{11} peaks confirm the presence of both metallic and semiconducting nanotubes in the film. In addition, the optical spectra were utilized to estimate the thickness of the film (h) derived from Lambert-Beer's law as

$$h = a_0 \log_{10} \xi, \quad 3.2-1$$

where a_0 is an attenuation coefficient, ξ is the transmittance.

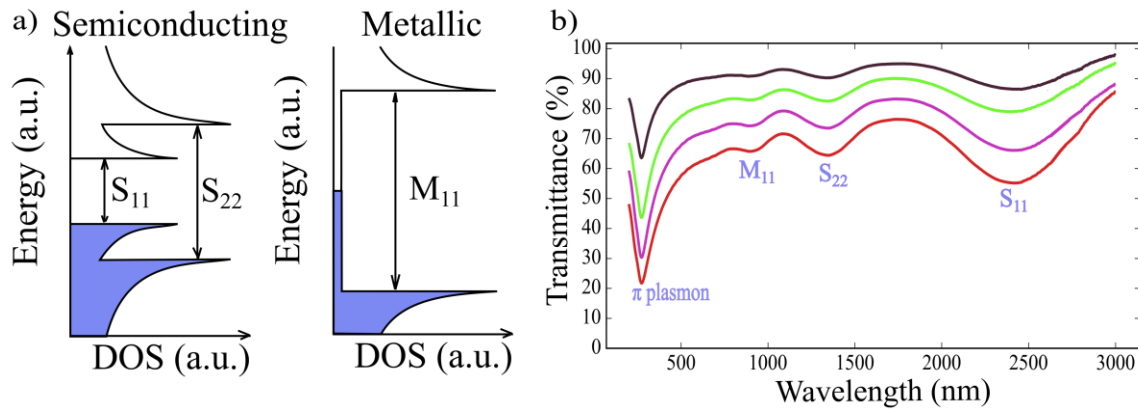


Figure 3.2-3. a) Electron density of states for semiconducting and metallic SWCNTs. b) Typical optical spectra of SWCNT films having different thicknesses.

3.2.4 Fourier-transform infrared spectroscopy

Fourier-transform infrared spectroscopy (FTIR) is widely used to obtain the absorption spectra of the substance in the infrared wavelength range and strive the similar goals as UV-vis-NIR spectroscopy^{83,84}. The FTIR is based on modulation of light source and simultaneous measurement of many wavelengths, unlike the double beam spectrometers where only one wavelength is measured at time. As a result, the measurements are performed rapidly. Typically, the FTIR utilize the Michelson

interferometer, where an incident beam from a source is divided with beam splitter into two coherent beams, which being reflected back from the mirrors interfere (Figure 3.2-4a). Movement of one of the mirrors introduces the signal modulation. The resulted signal after pathing through the sample records with a detector as a function of optical path difference. Finally, the Fourier transform of an interferogram gives the dependence of the transmitted signal in arbitrary units on the wavelength. The SWCNT film infrared absorption spectra (Figure 3.2-4b) were measured using Bruker Vertex 70v and obtained results were utilized for experiments on SWCNTs temperature measurements and for theoretical estimations of radiation dissipative channels in Sections 3.4 and 4.2.3.

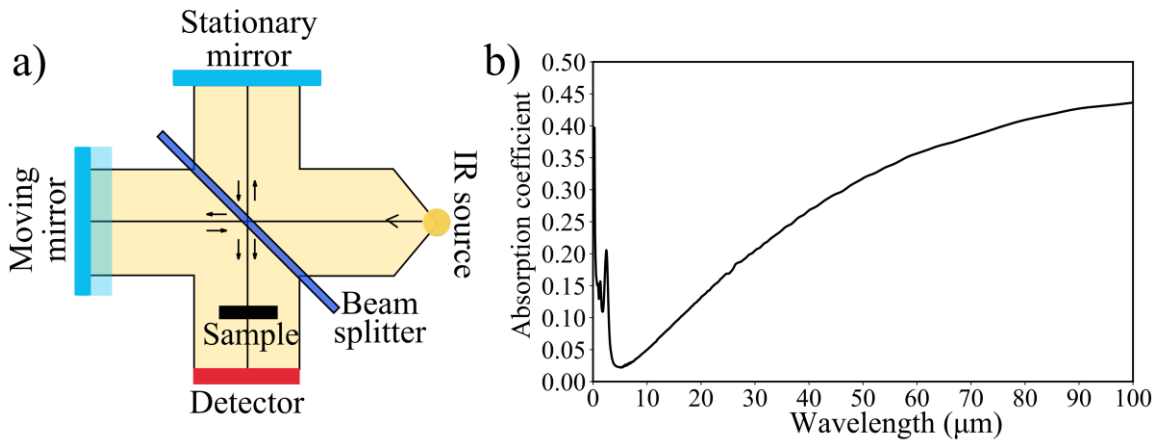


Figure 3.2-4. a) Principle scheme of Michelson interferometer. b) Typical infrared absorption spectrum of SWCNT film.

3.3 Sound measurements

The experimental setup for thermophone measurements was designed to measure the dependency of the sound pressure on the frequency and on the azimuth angle between

the sample and the microphone. The setup consisted of two parts: sound generation and sound detection (Figure 3.3-1). Both parts were computer controlled with a software written in Python programming language. In the experiments, the program made current frequency sweep from 0.5 to 50.5 kHz with a step of 1 kHz. For a certain frequency, the sound generation process was the following:

- 1) a sine wave was generated by a lock-in amplifier (Zurich instruments MFLI);
- 2) the wave was amplified by a high voltage amplifier (Falco systems WMA-300);
- 3) the sine signal reached the sample inducing Joule heating and, consequently, sound propagation, while the oscilloscope (Agilent DSO-X 3054A Digital Oscilloscope) controlled the signal shape;
- 4) a multimeter (Keithley 2000) measured the voltage and the current (by voltage drop via high power shunt resistor) on the sample using 2 channels (Keithley 2000-SCAN-901-01 card).

The detection process was as follows:

- 1) the signal was received with a microphone (B&K 4138-A-015, free-fields corrections were taken into account) and amplified with a low-noise preamplifier (Stanford research systems SR 560), which also filtered undesirable low and high frequencies;
- 2) the second harmonic of the original signal was measured with a lock-in amplifier (Zurich instruments MFLI) with the parameters controlled by the program for optimal measurements.

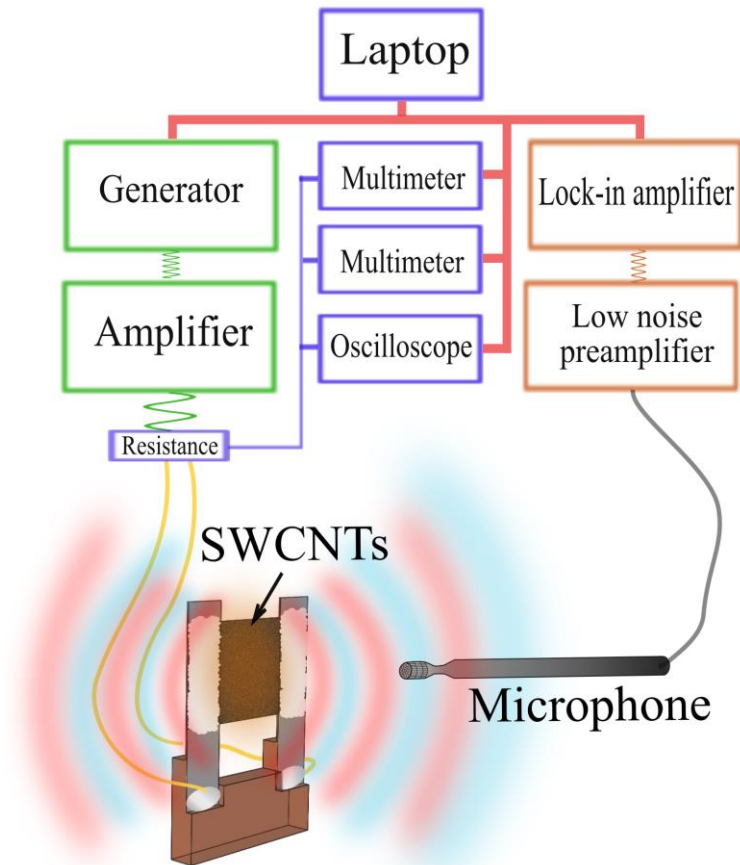


Figure 3.3-1. Schematic diagram of the experimental setup, where the power equipment marked by green color; the sound detection part by orange color and the signal acquisition part by purple color.

3.4 Temperature measurements

The temperature measurements of the sample in this work were performed at ambient conditions for thermophone characterization and under vacuum conditions to control the temperature during the purification process. For both cases, the temperature was controlled by the non-contact method based on measurements of radiation from the heated sample. The equipment for such type of measurements supply the emissivity

coefficient as a setting parameter and work in different spectral range, which depends on the range of temperature investigation.

In the thermophone characterization, the alternating current (AC) was applied to the free-standing film as described in Section 3.3. The average temperature on the surface of the sample under ambient conditions was measured by the infrared camera FLIR T650-sc. The camera works in the spectral range of 7-14 μm and measures temperature distribution on the sample surface in the range from -40°C to 650°C (Figure 3.4-1a). The camera was used to control temperature and adjust the input electric power to obtain the surface temperature of $\sim 80^\circ\text{C}$ which in turn allow to keep thermophones under the equal condition and compare the samples of different thicknesses.

The temperature control of the samples during purification in vacuum was carried out by pyrometer Euromix RXR 2300, which allowed to measure temperature from 600°C to 2300°C and worked in the spectral range from 1.0 to 1.6 μm . The experimental setup for vacuum purification by Joule heating included chamber equipped with KF flanges maintained under pressure $P \leq 10^{-3}$ Pa using Pfeiffer Hi-cube 80 vacuum pump and a pressure gauge Pfeiffer MPT100. The free-standing SWCNT films were heated by direct current (DC) with Electro Automatics 3200-04C utilizing four contact method of power implication (Figure 3.4-1b-c). The vacuum window between the sample and pyrometer was transparent in the pyrometer operation range.

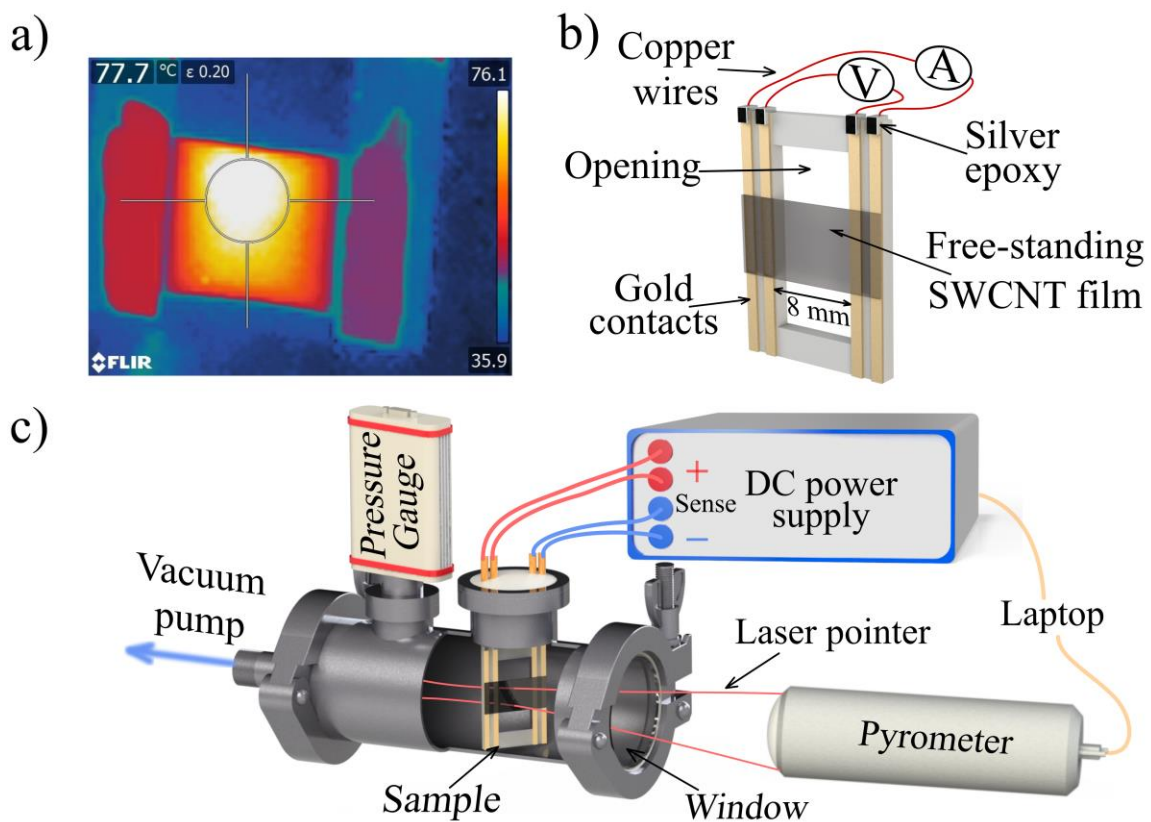


Figure 3.4-1. a) Typical temperature distribution on the surface of SWCNT film under ambient conditions measured with FLIR T650-sc. b) Free-standing SWCNT film sample ($8 \times 8 \text{ mm}^2$) mounted on a quartz glass substrate with a rectangular opening used for purification experiments. c) Schematic diagram of an experimental setup.

Chapter 4. Results and discussions

4.1 Theory of thermophones

The main limitation of current thermophone theory is the point-source approximation⁸⁵. It is not applicable when wavelengths (λ) become comparable or smaller than the size of the sample, which is especially significant for the ultrasound frequency. As a result, the theory predicts too high sound pressures. For instance, for the samples with the size of $1 \times 1 \text{ cm}^2$ the frequency of the transition from large to small wavelengths is 16 kHz. Here we extended theoretical approach to the case of source of finite size, comparable to the sound wavelength.

The thermal and acoustic parts of the problem can be solved separately at low frequencies $f \ll v_s^2 / \alpha_T$, where f is the frequency of the sound, v_s is the speed of sound, α_T is the thermal diffusivity⁸⁵. The logical sequence of our theory derivation is presented in Figure 4.1-1. Briefly, the oscillating in time heating results in the oscillating air pressure at the surface of the sample, which then converts into the propagating sound waves. One then needs to take into account the diffraction effects to obtain the measured sound pressure.

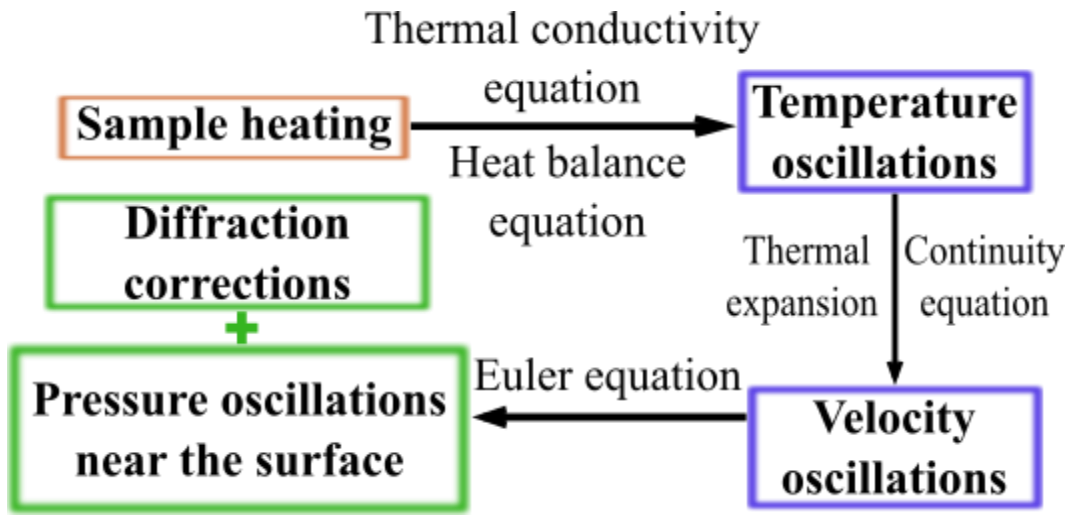


Figure 4.1-1. Diagram showing the principal steps in thermoacoustic theory derivation.

4.1.1 Temperature oscillations

In thermophones, temperature oscillations in time lead to a sound propagation. In order to find an amplitude of the temperature oscillations, T_{osc} , we consider an electrically conducting sample of thickness, h , and surface area, S . The sample is surrounded by air (Figure 4.1-2). When an alternating current with a frequency of $f/2$ passes through the sample, it causes oscillations in the power converted into the Joules heating of the sample:

$$P(t) = 2P_0 \sin^2(\pi ft) = P_0 - P_0 \cos(2\pi ft), \quad 4.1-1$$

where P_0 is the time averaged electrical input power, t is the time. The first (time independent) term in Equation 4.1-1, P_0 , induces Joule heating, which increases the temperature of the sample from the air temperature T_0 to the higher value T_{avg} (Figure 4.1-2). The second (time dependent) term in Equation 4.1-1 oscillating part of electrical

power, $P_0 \cos(2\pi ft)$, leads to periodic temperature oscillations with an amplitude T_{osc} , which we determine below.

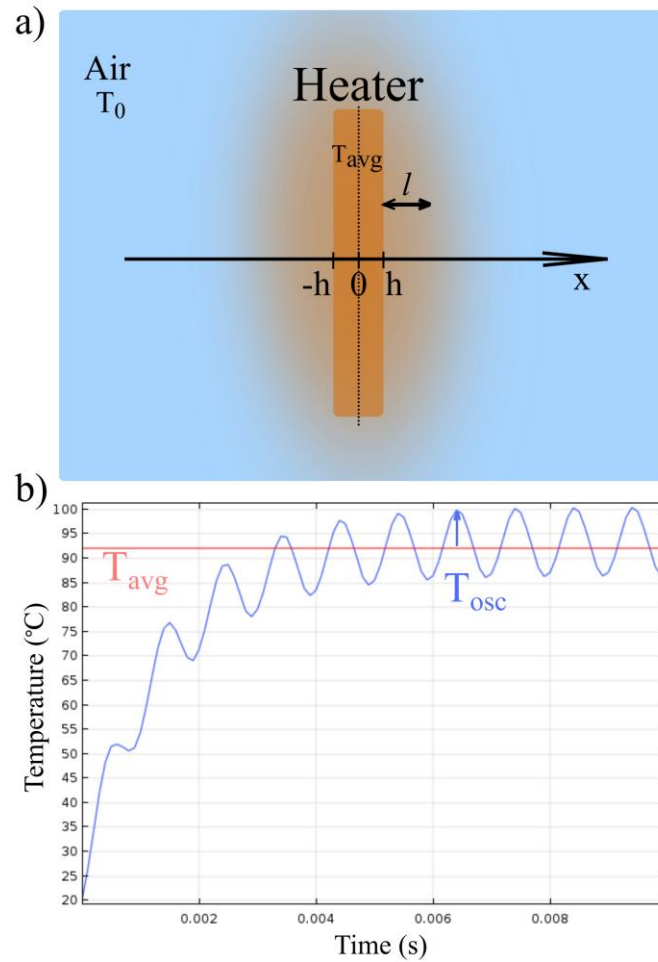


Figure 4.1-2. a) Heating illustration of the sample with a thickness of h , in air atmosphere. b) COMSOL calculations of temperature dependence on time, where red color corresponds to instantaneous stationary heating under power P_0 and blue corresponds to heating of the sample at $P_0 + P_0 \cos(2\pi ft)$.

To find T_{osc} , we consider the thermal conductivity equation

$$\rho_g C_g \frac{\partial \delta T(t,x)}{\partial t} = \kappa \Delta \delta T(t,x), \quad 4.1-2$$

where t is a time, x is the axis of the coordinate in the direction perpendicular to the sample surface, ρ_g is the air density, C_g is the heat capacity of air per unit mass, and κ is the thermal conductivity of air. Here, one-dimensional approximation was used to obtain the temperature oscillation, however the full geometry has to be considered in the case of strong effects of convection and heat conduction to the contacts.

We look for the solution of the form

$$\delta T(t,x) = T_{osc} e^{i(q(x-h/2)-\omega t)}, \quad 4.1-3$$

where q is the wave number, $\omega = 2\pi f$ is the angular frequency. Substituting Equation

4.1-3 into Equation 4.1-2 we obtain $q = \frac{(1+i)}{\sqrt{2}} \sqrt{\frac{\omega \rho_g C_g}{\kappa}}$. We also define the thermal diffusion

length

$$l(\omega) \equiv \frac{1}{\text{Im } q} = \sqrt{\frac{2\kappa}{\omega \rho_g C_g}}. \quad 4.1-4$$

The amplitude of temperature oscillations can now be found from the heat balance equation

$$\frac{P(t)}{S} = C_s \frac{\partial(\delta T(t,x))}{\partial t} - \kappa \frac{\partial(\delta T(t,x))}{\partial x}, \quad 4.1-5$$

where C_s is the heat capacity of the sample per unit area (HCPUA). It is defined as $C_s = \rho_h h C_h$, where ρ_h is the density of the sample, and C_h is the heat capacity of the sample per unit mass. Equation 4.1-5 neglects the effects of convection, black body radiation and heat

conduction to the electrical contacts. Substituting Equation 4.1-3 into Equation 4.1-5, we obtain

$$T_{osc} = \left| \frac{iP_0}{S(q\mu + \omega C_S)} \right|. \quad 4.1-6$$

In order to verify Equation 4.1-6 and approximations used above, we arranged numerical calculations in COMSOL software. The thermal conductivity equation of the used numerical model took into account the convection effect introduced in heat flux module of COMSOL by condition of natural convection on a vertical wall (see Section 4.2). The results of the calculations of temperature amplitude, T_{osc} , with COMSOL and Equation 4.1-6 for different values of the heat capacity per unit area found to be in a very good agreement, which proves the applicability of the approximations used in derivation of Equation 4.1-6 (Figure 4.1-3).

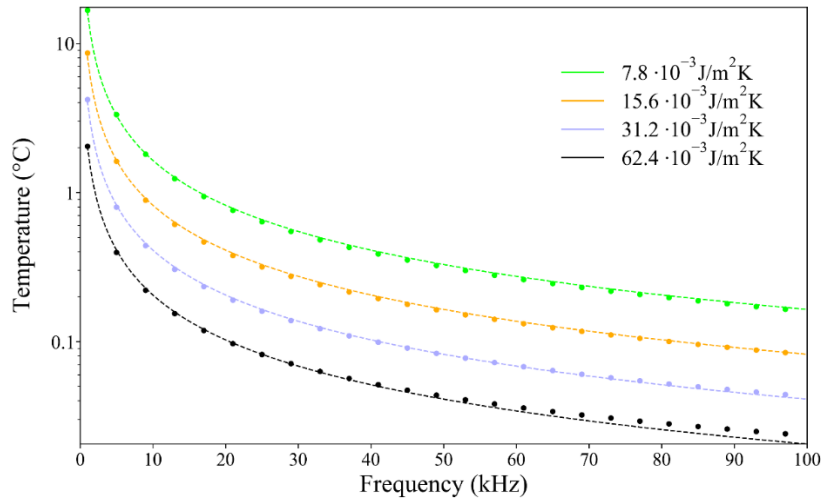


Figure 4.1-3. Dependence of temperature amplitude T_{osc} on the applied alternating current frequency for films of different heat capacity per unit area. The dashed lines correspond to Equation 4.1-6, while the dots were calculated using COMSOL software by a finite element method.

4.1.2 Density and velocity oscillations near the sample surface

The oscillations of air temperature near the surface of the sample lead to the oscillations of pressure p , and density ρ , within a layer of characteristic length $l(\omega)$. In general, the density variation $\delta\rho$, caused by changes in pressure δp , and temperature δT , can be expressed in the linear approximation as:

$$\delta\rho = \rho_g(\beta\delta p - \alpha\delta T), \quad 4.1-7$$

where α is the thermal expansion coefficient, β is the compressibility. The latter two are defined as $\alpha \equiv -\frac{1}{\rho_g}\left(\frac{\partial\rho_g}{\partial T}\right)_p$ and $\beta \equiv \frac{1}{\rho_g}\left(\frac{\partial\rho_g}{\partial p}\right)_T$. Since, for the ideal gas, $p = \rho RT$, Equation 4.1-7 takes the form

$$\delta\rho = \rho_g\left(\frac{\delta p}{p_0} - \frac{\delta T}{T_0}\right). \quad 4.1-8$$

In Equation 4.1-8 the term, $\delta p/p_0$, can be neglected, because it is several orders of magnitude smaller than $\delta T/T_0$. The reason for this smallness is that the pressure adjusts to the change of external conditions ballistically with characteristic time of l/v_s , while the temperature adjusts diffusively on a much slower timescale of $1/\omega$. This smallness is also the subject to the final consistency check after the amplitude of the pressure oscillations is obtained. Equation 4.1-8 then translates into the following time dependent relation for the density oscillations

$$\delta\rho(t, x) = -\rho_g\left(\frac{\delta T(t, x)}{T_0}\right). \quad 4.1-9$$

The above density oscillations can now be converted into the oscillations of the gas velocity field $u(t, x)$. The velocity oscillations can be obtained with the help of the continuity equation

$$\frac{\partial \rho}{\partial t} = -\rho_g \frac{\partial u}{\partial x}. \quad 4.1-10$$

The substitution of Equation 4.1-9 and 4.1-3 into Equation 4.1-10 then gives

$$\frac{\partial u}{\partial x} = \frac{-i\omega\rho_g\delta T(t,x)}{T_0}. \quad 4.1-11$$

Integrating Equation 4.1-11 with respect to x , we obtain the asymptotic value of the amplitude of air velocity oscillations outside of the diffusive heating layer near the surface

$$u_0 = \frac{-i\omega}{T_{avg}} \int_{h/2}^{d_{int}} \delta T(t, x) dx = \frac{\omega T_{osc}}{qT_0}, \quad 4.1-12$$

where the origin of the x -axis is defined in Figure 4.1-2 and $l(\omega) \ll d_{int} \ll \lambda$, in air for the frequency range from 1kHz to 100 kHz, $l(\omega) \in [81.9, 8.2] \mu m$, $\lambda \in [34.3, 0.3] cm$. The result obtained in Equation 4.1-12 agrees with the general concept of perturbation modes^{86,87}.

4.1.3 Pressure oscillations near the sample surface

The sound pressure can now be found from the velocity field using the Euler equation for a compressible fluid without dissipation:

$$\frac{\partial u}{\partial t} + (u\nabla)u = -\frac{1}{\rho_g} \nabla p. \quad 4.1-13$$

To calculate the sound pressure near the sample surface we approximate our sample with a spherical transducer of the same surface area as discussed in section 4.1.4. Let us

now consider a solution of the Euler equation in a semi-open spherical geometry, namely, outside of the spherical boundary of radius a . For small variations of the density and pressure, and for $u \ll v_s$, the boundary condition on the spherical surface is

$$\left. \frac{d\vec{u}}{dt} \right|_{r=a} = -\frac{1}{\rho_g} \left. \frac{dp}{dr} \right|_{r=a}. \quad 4.1-14$$

We look for the solution of the form

$$p = A \frac{e^{i(kr-\omega t)}}{r}, \quad 4.1-15$$

where r is the distance from the center of the sphere ($r \geq a$) and A is a constant. In Equation 4.1-15 in order to simplify subsequent notations, we switch from δp to p to represent small deviation from the equilibrium pressure p_0 .

Substituting $\left. \frac{du}{dt} \right|_{r=a} = i\omega u_0$ and 4.1-15 into 4.1-14, we obtain

$$-i\omega u_0 = \frac{A}{\rho_g} \left(\frac{ika-1}{a^2} \right), \quad 4.1-16$$

which in turn gives

$$|A| = \frac{\omega u_0 \rho_g a^2}{\sqrt{(ka)^2 + 1}}. \quad 4.1-17$$

Equation 4.1-17 applies to both small ($ka \ll 1$) and large ($ka \gg 1$) thermophones. After the velocity field from Equation 4.1-12 and $k = 2\pi f/v_s$ are substituted in Equation 4.1-17 and the result is further substituted in Equation 4.1-15, we obtain the root-mean squared sound pressure of a spherical transducer.

$$p_{rms}(f, r) = \frac{fP_0}{2\sqrt{2}c_g T_0 r} \frac{1}{\sqrt{\left(\frac{2\pi a f}{v_s}\right)^2 + 1}} \frac{1}{\sqrt{2\chi^2(f) + 2\chi(f) + 1}}, \quad 4.1-18$$

where $\chi(f) = \frac{h\rho_h c_h}{l(2\pi f)\rho_g c_g}$. Here $l(2\pi f)$ is the function of frequency defined by Equation 4.1-4. The function $\chi(f)$ is responsible for switching between the Arnold and Xiao theoretical limits, which were discussed in Section 2.3. Therefore, in the limit $\chi(f) \approx 0$, the Equation 4.1-18 turns to Xiao theoretical limit ($p \sim f/C_s$), whereas in the limit $\chi(f) \gg 1$, it turns to Arnolds theoretical limit ($p \sim \sqrt{f}/C_g$).

4.1.4 Flat transducers and intensity gain

The result for the spherical transducer given by Equation 4.1-18 can now help us to obtain the sound pressure for a flat transducer of an arbitrary shape. In general, there are three regimes of the flat-transducer operation, which depend on the ratio between the sound wavelength and the characteristic sample size: (i) the regime of a point source when the wavelength much larger than the sample size, (ii) the regime of a large source when the wavelength much smaller than the sample size and (iii) the intermediate regime of finite source when the wavelength comparable with the sample size.

For a point source the result for the spherical transducer given by Equation 4.1-18 applies entirely, using effective radius

$$a = \sqrt{S/4\pi}, \quad 4.1-19$$

where S is the double-sided surface area of the flat transducer.

For a large source the isotropic spherical pressure front, given by Equation 4.1-18, must be modified to account for the directivity of the sound emission as described below. However, in this case, the value of the pressure for the spherical transducer near the spherical surface, $p_{rms}(f, a)$ can still be used to obtain the pressure of the flat transducer near the flat surface again with the effective radius given by Equation 4.1-19.

In the intermediate regime, strictly speaking, one needs to perform the complete numerical simulation of the coupled thermoacoustic equations, and we have indeed done this using COMSOL software as described below. However, we have found that, at least for the transducers of square shape, the intermediate regime is very well described by the preceding prescription for large transducers in combination with the intensity gain calculation described below.

Intensity gain function is the ratio of intensity in a certain direction to the isotropically averaged intensity

$$G(r, \varphi, \theta) = \frac{I(r, \varphi, \theta)}{\frac{1}{4\pi} \int_0^{2\pi} \int_0^\pi I(r, \varphi', \theta') \sin \theta' d\varphi' d\theta'} \quad 4.1-20$$

where $I(r, \varphi, \theta)$ is the sound intensity, φ and θ are the azimuth and polar angles. The intensity distribution on the sphere of radius, r , surround the sample is proportional to the square of the sound pressure $p^2(r, \varphi, \theta)$.

In order to find $p(r, \varphi, \theta)$ we used Huygens-Fresnel principle, i.e. each point on the transducers surface was assumed to be a point source of spherical waves, $p_i = A_i \frac{e^{-ikr_i}}{r_i}$ (Figure 4.1-4). The intensity of this point sources was chosen using the result for

the spherical transducer and Equation 4.1-18. The results for the intensity gain calculation in front of the sample is presented in Figure 4.1-5.

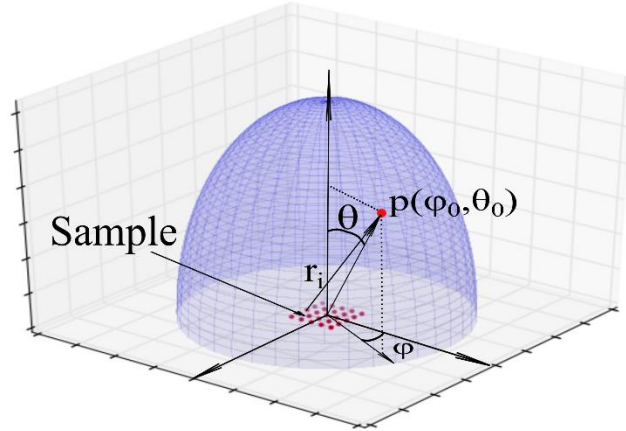


Figure 4.1-4. Spherical surface used for calculation of the intensity gain function.

The calculation of intensity gain function of Equation 4.1-20 by Huygens-Fresnel principle includes the transition from the near to the far field with an increase of the sphere radius. In order to verify these numerical results, we compared them with the analytical result for the directivity of a square emitter in the far field:

$$D(\varphi, \theta) = \text{sinc}\left(\frac{k \sin \theta \cos \varphi L}{2}\right) \text{sinc}\left(\frac{k \sin \theta \sin \varphi L}{2}\right), \quad 4.1-21$$

where $\text{sinc}(x) \equiv \frac{\sin(x)}{x}$, L is the edge lengths of the square transducer. Experimentally the directivity function was verified for rectangular thermophone by Vesterinen *et al.*¹⁹. The intensity gain is then calculated as:

$$G(\varphi, \theta) = \frac{D^2(\varphi, \theta)}{\frac{1}{4\pi} \int_0^{2\pi} \int_0^\pi D^2(\varphi', \theta') \sin \theta' d\varphi' d\theta'}. \quad 4.1-22$$

As seen in Figure 4.1-5 the analytical result of Equation 4.1-22 is in excellent agreement with the numerical calculation for large distances from the source.

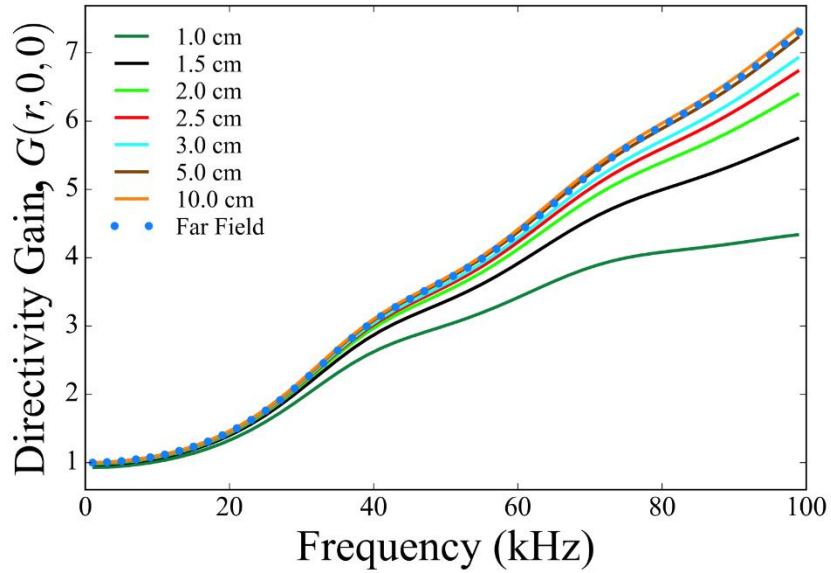


Figure 4.1-5. Dependence of the intensity gain function on frequency. Solid lines represent intensity gain $G(r,0,0)$ for different sphere radius calculated using Equation 4.1-20 and Huygens-Fresnel principle. Dots line is a far field calculation of intensity gain $G(0, 0)$ performed in accordance with Equation 4.1-22.

Finally, the sound pressure of the flat thermophone is defined combining Equations 4.1-18, 4.1-19 and 4.1-20

$$p_{rms}(r, f, \varphi, \theta) = \frac{fP_0}{2\sqrt{2}c_g T_0 r} \frac{1}{\sqrt{\left(\frac{Sf}{2v_s}\right)^2 + 1}} \frac{\sqrt{G(r, \varphi, \theta)}}{\sqrt{2\chi^2(f) + 2\chi(f) + 1}} \quad 4.1-23$$

One should note that the problem of thermophones is similar to photoacoustic transducers. The analogy may be successfully applied in description of thermophones, especially under pulse signals⁸⁸.

4.1.5 Volumetric heaters

Sections 4.1.1-4.1.4 cover the thermophone theory for the case of flat thermophone. For the flat thermophone the gas molecules interact with the surface of the sample and pressure oscillation takes place near the surface of the sample within the layer of characteristic thickness of $l(\omega)$. However, in the case of materials, where gas molecules are able to penetrate inside the volume of the sample, like for aerogel materials, the characteristic length involved in sound generation turns to $h/2 + l(\omega)$. Such thermophones are called volumetric.

The general ideas in theoretical derivations of the sound pressure for the volumetric thermophones are the same as that for the flat. Here we discuss the modifications of flat thermophones theory including thermal conductivity equation (Equation 4.1-2), heat balance equation (Equation 4.1-5) and velocity field (Equation 4.1-12) to obtain volumetric thermophone sound pressure.

For volumetric heaters the heat conductivity problem is divided into heat conductivity inside and outside the heater and defines by system of equations,

$$\begin{cases} \rho_g C_g \frac{\partial T_1(t,x)}{\partial t} = \kappa \Delta T_1(t,x) + Q, & |x| \leq h/2 \\ \rho_g C_g \frac{\partial T_2(t,x)}{\partial t} = \kappa \Delta T_2(t,x), & h/2 < |x| < \infty \end{cases} \quad 4.1-24$$

Where Q is a volumetric heat density, $T_1(t, x), T_2(t, x)$ are respectively amplitudes of temperatures oscillations inside and outside the sample. Equation 4.1-24 assumes the same gas properties inside and outside the aerogel structure. In the case of dense aerogel structures (high volume fraction) and small pores size, the gas properties inside the pores of sample differ from those for free space^{89,90}. The heat balance equation of volumetric heater takes the form

$$\frac{P(t)}{V} = C_V \frac{\partial(\delta T(t, x))}{\partial t} + Q, \quad 4.1-25$$

where V is the sample volume, C_V is heat capacity per unit volume. Substituting Equation 4.1-25 into Equation 4.1-24 one can obtain the system of heat conductivity equations

$$\begin{cases} (\rho_g C_g + C_V) \frac{\partial T_1(t, x)}{\partial t} = \kappa \Delta T_1(t, x) + \frac{P(t)}{V}, & 0 \leq |x| \leq h/2 \\ \rho_g C_g \frac{\partial T_2(t, x)}{\partial t} = \kappa \Delta T_2(t, x), & h/2 < |x| < \infty \end{cases} \quad 4.1-26$$

We look for the solution of Equation 4.1-26 in the form

$$\begin{cases} T_1(t, x) = A(e^{i(q_1 x - \omega t)} + e^{-i(q_1 x - \omega t)}) + \frac{iP(t)}{-i\omega(\rho_g C_g + C_V)V}, & |x| \leq h/2 \\ T_2(t, x) = B e^{i(q_2 x - \omega t)}, & h/2 < |x| < \infty \end{cases}, \quad 4.1-27$$

Substituting Equation 4.1-27 into Equation 4.1-26 we obtain $q_1 = \frac{(1+i)}{\sqrt{2}} \sqrt{\frac{\omega(\rho_g C_g + C_V)}{\kappa}}$ and $q_2 = \frac{(1+i)}{\sqrt{2}} \sqrt{\frac{\omega \rho_g C_g}{\kappa}}$. Parameters A and B, in turn, are defined by substituting Equation 4.1-27 into the system of boundary conditions, which corresponds to the continuity of temperature and heat flux on the sample surface

$$\begin{cases} T_1(t, h/2) = T_2(t, h/2) \\ \kappa \frac{dT_1(t, x)}{dx} \Big|_{x=h/2} = \kappa \frac{dT_2(t, x)}{dx} \Big|_{x=h/2} \end{cases} \quad 4.1-28$$

Substituting Equation 4.1-27 into Equation 4.1-28 lead to

$$\begin{cases} A = \frac{P(t)}{-\omega(\rho_g C_g + C_V)V \left(\frac{q_1}{q_2} (e^{iq_1 h/2} - iq_1 e^{-iq_1 h/2}) - (e^{iq_1 h/2} + e^{-iq_1 h/2}) \right)} \\ B = \frac{q_1 A * (e^{iq_1 h/2} - iq_1 e^{-iq_1 h/2})}{q_2 e^{-iq_2 h/2}} \end{cases} \quad 4.1-29$$

In case of volumetric heater, gas molecules penetrates inside the heater volume and Equation 4.1-12 for air velocity take the form

$$u_0 = \frac{-i\omega}{T_{avg}} \left(\int_0^{h/2} T_1(t, x) dx + \int_{h/2}^{\infty} T_1(t, x) dx \right) \quad 4.1-30$$

Substitution of Equation 4.1-29 and 4.1-27 into 4.1-30 results in the piston velocity of volumetric thermophone

$$u_0 = \frac{hP_0}{2T_{avg}(\rho_g C_g + C_V)V} \left(1 - \frac{2(e^{iq_1 h/2} - e^{-iq_1 h/2})}{q_1 h} \frac{C_V / \rho_g C_g}{(1 - q_2/q_1)e^{iq_1 h/2} + (1 + q_2/q_1)e^{-iq_1 h/2}} \right) \quad 4.1-31$$

Finally, the sound pressure of the volumetric heater near the surface is defined by substituting Equations 4.1-31 and 4.1-17 into Equation 4.1-15

$$p_{rms}(f, r) = \frac{f \rho_g P_0}{2r T_0 (\rho_g C_g + C_V)} \left(1 - \frac{2(e^{iq_1 h/2} - e^{-iq_1 h/2})}{q_1 h} \frac{C_V / \rho_g C_g}{(1 - q_2/q_1)e^{iq_1 h/2} + (1 + q_2/q_1)e^{-iq_1 h/2}} \right) \sqrt{\frac{G(r, \varphi, \theta)}{\left(\frac{2\pi a f}{v_s}\right)^2 + 1}} \quad 4.1-32$$

According to the theoretical analysis of Equation 4.1-32, the volumetric effect takes place in the films with the thickness of at least a few micrometers and increases the sound

pressure because of suppression of the heat accumulation effect. To demonstrate the effect, we fixed the mass of the sample to be $0.5 \mu g$ and vary the thickness of the film from 1 to $500 \mu m$ making thermophones sparser (Figure 4.1-6). The results address the significant increase in sound pressure along with the sample thickness. For samples with thickness less than $1 \mu m$, the volumetric effect is negligible and sound pressure matches the limit of sound pressure for flat thermophone defined by Equation 4.1-18. Moreover, samples with the thickness of $100 - 500 \mu m$ reach ultimate limit for sound pressure of thermophones defined by Equation 4.1-32 in the limit of $C_V = 0$. Overall, the volumetric effect increases efficiency of thermophone and the most efficient thermophones should be as sparser as possible, at least for thickness much less than the sound wavelength.

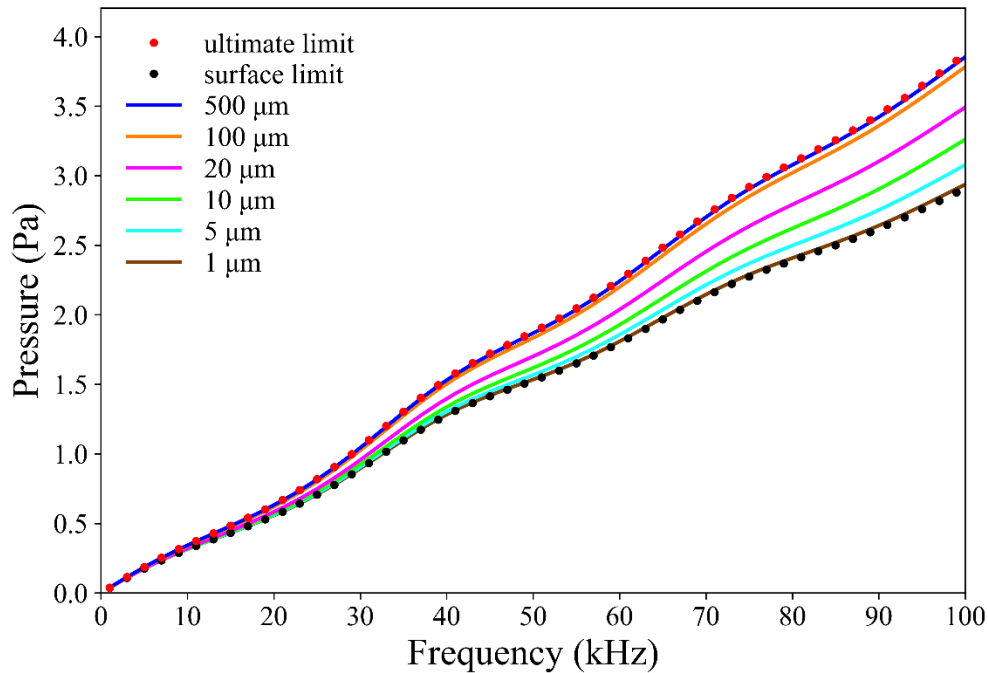


Figure 4.1-6. Theoretically predicted dependence of sound pressure on frequency for the volumetric samples of different thickness with the size of $1 \times 1 \text{ cm}^2$ and mass of $0.5 \mu\text{g}$. An ultimate limit of sound pressure corresponds to red dots, while a surface limit corresponds to black dots.

4.1.6 Numerical model of thermophone

In order to confirm the theoretical approaches used in derivation of Equation 4.1-23, we modeled our system using the COMSOL Multiphysics 5.3a software. In our modeling, we used the acoustics module of COMSOL in a spherical region of space with the radius of 3 cm, which had a bordering layer where the “perfectly matched layer” routine was applied. A smaller cuboid region of sizes 1.25 cm x 1.25 cm x 0.2 cm was placed within the above spherical region, which contained a square emitter of size 1 cm x 1 cm. In this rectangular region the acoustic module implemented thermoviscous acoustic

simulations of the linearized Navier-Stocks equation, while in the entire spherical region it implemented acoustic pressure simulations using Helmholtz equations. Input for the simulations included temperature oscillation on the surface of $1 \times 1 \text{ cm}^2$ described by Equation 4.1-6. The sketch of the overall simulation is shown in Figure 4.1-7. The principal geometry of the COMSOL modeling, including thermoviscous acoustic module, pressure acoustic module and perfectly matched layer.

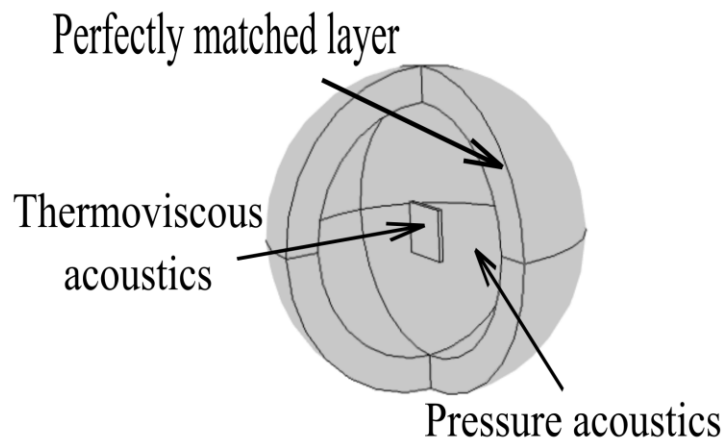


Figure 4.1-7. The principal geometry of the COMSOL modeling, including thermoviscous acoustic module, pressure acoustic module and perfectly matched layer.

The discretization mesh had at least 30 finite elements per wavelength, which led to significant calculation complexity at high frequencies. To overcome this problem, we used symmetric boundary conditions and directly modeled one-fourth of the space shown in the Figure 1.5-7. In the simulations we used the generalized minimal residual (GMRES) method with the parallel direct sparse solver (PARDISO) as a direct preconditioner.

4.2 Temperature control of SWCNT films: theory and experiment

In this section we discuss approaches to calculate the temperature on the surface of SWCNT film under the impact of Joule heating. Cases of ambient and vacuum conditions were considered. Ambient conditions were utilized in calculations to obtain temperature of thermophones during sound measurements. Whereas, vacuum conditions were employed to verify temperature in Joule-assisted purification. In order to model the thermal processes caused by Joule heating in SWCNT films, we utilized commercially available COMSOL Multiphysics 5.3a software. The COMSOL implements the finite difference method for the solution of differential equations and allows solving coupled problems, such as Joule heating.

In order to precisely estimate the temperature of free-standing film and energy dissipation, one should balance the input electrical power (P_{el}) applied by DC with powers dissipated because of the convection (P_{conv}), conduction (P_{cond}), and radiation effects (P_{rad}) (Figure 4.2-1a):

$$P_{el} = P_{conv} + P_{cond} + P_{rad}. \quad 4.2-1$$

To demonstrate the role of each of the heat dissipation channel we consider a 50 nm x 1 cm x 1 cm SWCNT film under impact of Joule heating. Results obtained in numerical calculation provide insight into roles of heat dissipation channels under vacuum and ambient conditions. At ambient conditions, the heat dissipation by convection dominates (Figure 4.2-1b) and at low input power takes over 80% of total power. For vacuum, the most energy dissipates by radiation, which at high input power takes over 90%

of total power (Figure 4.2-1c). It is noteworthy that the bottom line in the results is free-standing architecture of the samples in this work. In case of SWCNT films on the substrate it is essential to take into account the heat dissipation by conductivity into the substrate.

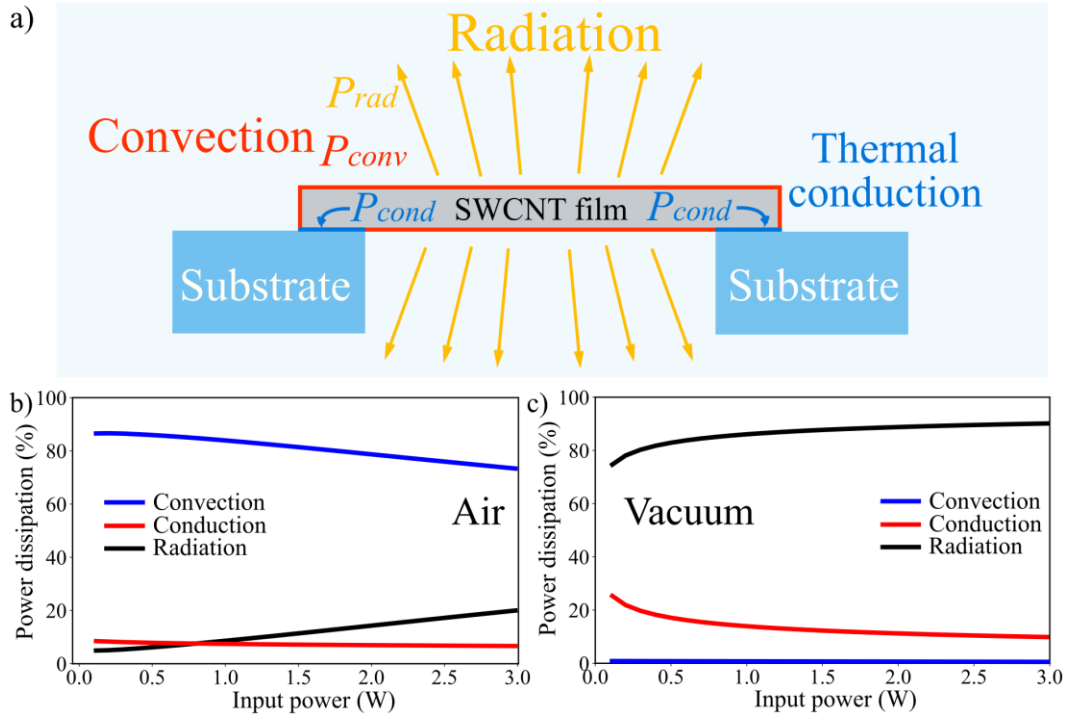


Figure 4.2-1. a) Illustration of power dissipation channels of a resistively heated SWCNT film. The dependence of power dissipation by convection, radiation and conduction on the input power in b) air and c) vacuum.

4.2.1 Energy dissipated by convection effect

The convection includes fluid motion as a bulk (advection) and random molecular motion (diffusion or conduction)⁹¹. In the case of the partial vacuum, the advection is absent and thermal conductivity depends on the surrounding pressure. The pressure-dependent conductivity – the Smolkovsky effect⁹² – is due to the comparability of the molecular mean free path and the size of confined space (*i.e.* the vacuum chamber). The

thermal conductivity increases with pressure until it reaches a constant value. The reason for that is a difference in the molecular motion: at low pressure it switches from the free-molecular ($\lambda \gg d$) to the continuum ($\lambda \ll d$) regime⁹². The characteristic parameter describing the transition is Knudsen number ($Kn = \lambda/d$, where λ is a molecule mean free path and d is the size of the confined space). Based on the molecular theory of gases, one can derive:

$$\lambda = \frac{2k_B T}{\sqrt{2}\pi d_m^2 P} \quad 4.2-2$$

where k_B is the Boltzmann constant, T is the sample temperature, P is the gas pressure, d_m is the kinetic diameter of gas molecule. At the pressure of 10^{-3} Pa in our system at sample's temperature equal to room temperature $Kn \approx 205$ and at $T = 1600^\circ\text{C}$ $Kn \approx 1400$. For the free molecular regime ($Kn > 10$), thermal conductivity in the vacuum is approximated as⁹²:

$$k_{vac} = \frac{k_{air}}{1 + 2\beta_t Kn} \quad 4.2-3$$

where k_{air} is the thermal conductivity of air at ambient pressure, β_t represents the “amount of energy transfer between the gas molecule and the solid material”⁹² estimated as:

$$\beta_t = \frac{1 - a_c}{a_c}, \text{ where } a_c = \frac{C_i m_r}{(1 + m_r)^2} \quad 4.2-4$$

where a_c is the thermal accommodation coefficient, m_r is the ratio of the gas to solid atomic masses, C_i is the empirical constant. The dependence of thermal conductivity on

the ambient pressure obtained from Equation 4.2-3 for several sample temperatures is presented in Figure 4.2-2a.

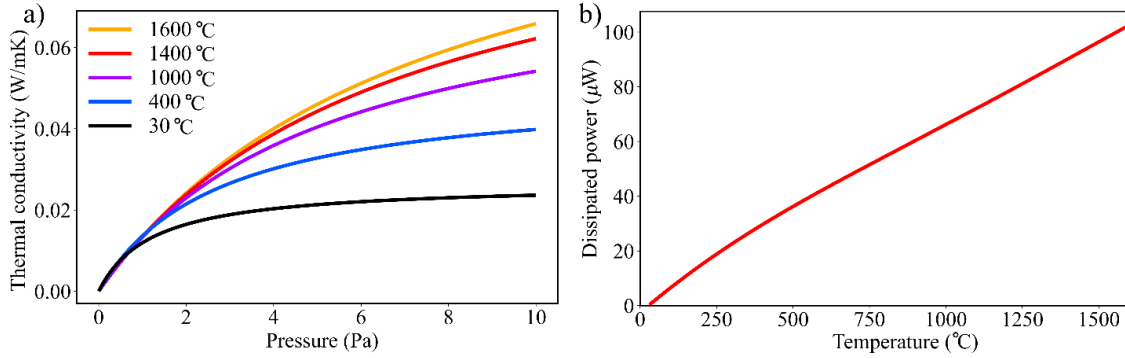


Figure 4.2-2. a) The dependence of thermal conductivity on ambient pressure for several temperatures. b) The dependence of dissipated power on temperature calculated with Equation 4.2-5 under pressure of 10^{-3} Pa.

In order to estimate the dissipated power from the film with a surface area of S , we used the following equation⁹³:

$$P_{conv} = Sk_{vac} \frac{(T - T_0)}{d} \quad 4.2-5$$

where d is the characteristic dimension of the confined space, T_0 is the temperature of the chamber wall. Thus, we calculated the dependence of P_{conv} on the temperature in the range from 30 to 1600 °C using Equation 4.2-5. It should be noted that the maximum power dissipated in a system under experimental conditions during the Joule assisted purification (see Section 4.4.1) is less than 10^{-4} W which is negligible amount compared to the experimental input power (1–12 W).

To obtain temperature at ambient conditions the thermal conductivity equations were solved numerically. To take into account the advection effect, the heat transfer coefficient from the film, h_{conv} , was approximated by conditions of natural free convection on a vertical wall⁹⁴

$$h_{conv} = \frac{k_{air}}{L} \left\{ 0.68 + \frac{0.67Ra^{1/4}}{\left(1 + \left(\frac{0.492k_{air}}{\mu C_p}\right)^{9/16}\right)^{4/9}} \right\} \quad 4.2-6$$

where L is the wall length, Ra is a Rayleigh number, μ is a dynamic viscosity of air, C_p is a specific heat capacity of external fluid at a constant pressure. Using the heat transfer coefficient one can show, that the convection heat dissipation dominates at ambient conditions over the radiation and heat conduction (Figure 4.2-1b). The Joule heating in air with input powers densities of 1.5-3.0 W/cm² lead to high average temperature (~350 – 600°C) on the surface of the SWCNT films, which for real system results in oxidization of the CNTs.

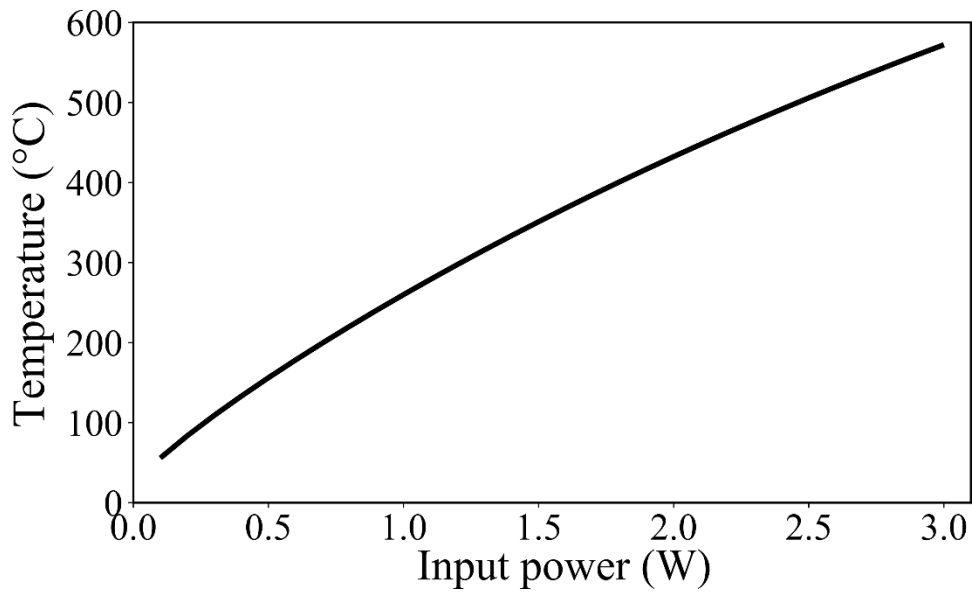


Figure 4.2-3. The dependence of average sample temperature on power for a free-standing sample with size of 50 nm x 1 cm x 1 cm under Joule heating in air.

4.2.2 Energy dissipated by thermal conductivity

In order to estimate the energy transferred to the electrical contacts (P_{cond}) (by means of thermal conduction), we arranged numerical simulations. The SWCNT film was modeled as a solid object with varying cross-section of 8 cm x h nm and the thermal conductivity of 600 W/m·K, which is the maximum value for the SWCNT films reported in the recent review⁹⁵. Therefore, we estimated the influence of P_{cond} on the temperature of the SWCNT film. As far as the thickness of the SWCNT films in the model is in the range of 40 – 1000 nm and the width and length are of 8 x 8 mm², we utilized two dimensional (2D) model of the sample due to a small temperature variation in the out-of-plane direction. Therefore, the modeling was performed in the 2D domain and included boundary conditions of temperature and diffuse surface. According to the calculations, the

effect of the heat conduction to the substrate (contacts) is almost negligible for the SWCNT films used for purification experiments (8 mm x 8 mm x 50 nm) (Figure 4.2-4b,c).

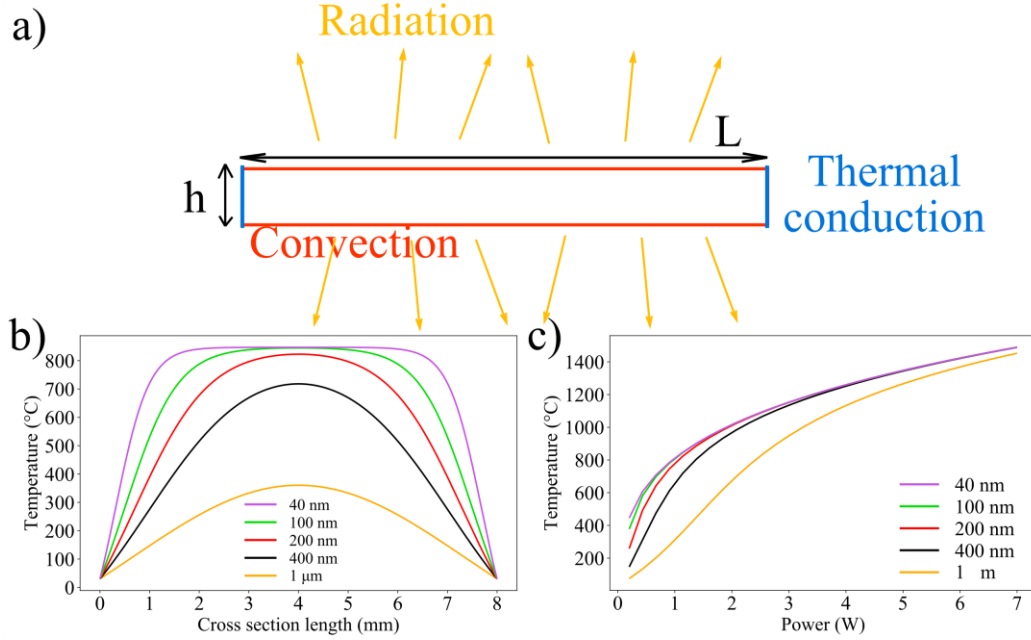


Figure 4.2-4. a) Schematic representation of the geometry used for the COMSOL simulation with boundary conditions of radiation and thermal conduction. b) The temperature dependence on the cross-section length under the impact of 1 W of electrical power for several sample thicknesses. c) The temperature in the middle of the SWCNT film with different thicknesses as a function of the input electrical power.

4.2.3 Energy dissipated from SWCNT film by the radiation effect

The amount of power dissipated by radiation at a given temperature described by:

$$P_{rad} = S \int_0^{\infty} \alpha(\lambda)(f(\lambda, T) - f(\lambda, T_0)) d\lambda, \quad 4.2-7$$

where S is the sample surface area, λ is the wavelength, $a(\lambda)$ is the absorption coefficient dependence on the wavelength, T is the temperature of the body, T_0 is the temperature of the surrounding media and $f(\lambda, T)$ is a Planck function defined as:

$$f(\lambda, T) = \frac{2hc^2}{\lambda^5} \frac{1}{\exp\left(\frac{hc}{\lambda k_B T}\right) - 1}, \quad 4.2-8$$

where h is the Planck constant, c is the speed of light, k_B is the Boltzmann constant. To obtain the temperature on the surface of the SWCNT film, we numerically solved the Equation 4.2-7 assuming $P_{rad} = P_{el}$. The resulted temperature turned to be in a very good agreement with the experimentally measured values.

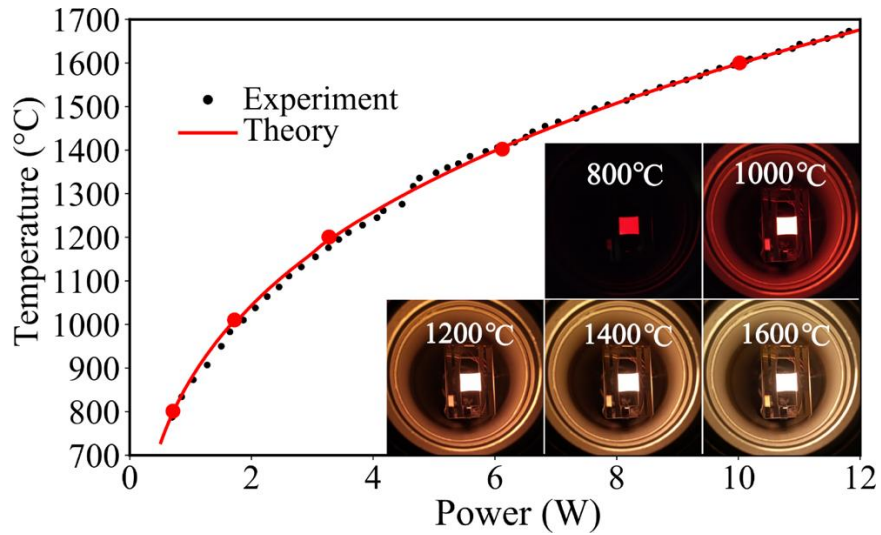


Figure 4.2-5. The comparison between experimental and theoretical dependence of SWCNT film temperature on the input electrical power. The insert images are the sample under the impact of the corresponding power.

4.3 Highly efficient thermophones based on SWCNT films

This section presents the systematic investigation of the thermophones performance of SWCNT films as a function of their thickness. The experiments were carried out in the frequency range from 1 kHz to 100 kHz. The record thermoacoustic performance of the freestanding SWCNT films showed four times higher efficiency in comparison with other thermophone materials under equivalent conditions. In addition, theoretically introduced volumetric effect in Section 4.1.5, was observed experimentally and is discussed in this section.

4.3.1 Amplitude frequency response of SWCNT based thermophones

From the above discussions in Section 4.1 it is now clear that decreasing of HCPUA (C_s) leads to higher sound pressure in thermophones. The fact is governed by an increase of $\chi(f)$ with HCPUA decreasing in Equation 4.1-23, which results in a decrease of sound pressure. To verify this dependence, the SWCNT films with different HCPUA were fabricated using the dry-transfer technique⁶⁹. The films HCPUA was controlled by the thickness of the films: $C_s \sim h$. The SWCNT films were suspended in a free-standing state between two aluminum strips and then covered with a silver paste, for a better electrical contact (see Figure 4.3-1)⁷⁰. Sample size was fixed to be 1x1 cm². Fabricated films had equal density due to specifics of the synthesis process and different thicknesses. Higher thickness corresponded to lower optical transmittance. In the experiments, we used films with the following values of transmittances at wavelength of 550 nm: 95%, 90%, 85%,

80%, 70%, and 60%, which corresponded to HCPUA of 2.9, 6.0, 9.3, 12.7, 20.4, 30.2 ($\times 10^{-3} J/m^2 K$) obtained as $C_s = C_h \rho_a$, where $C_h = 0.72 J/gK$ and

$$\rho_a = \rho_{a_{0.5}} \frac{\log_{10}(\xi)}{\log_{10}(0.5)}, \quad 4.3-1$$

where ξ is the film optical transmittance and $\rho_{a_{0.5}} = 5.5 \mu g/cm^2$ ⁹⁶. The samples were labeled by the percent values of their optical transmittances at wavelength of 550 nm, for instance: SWCNT-N%.

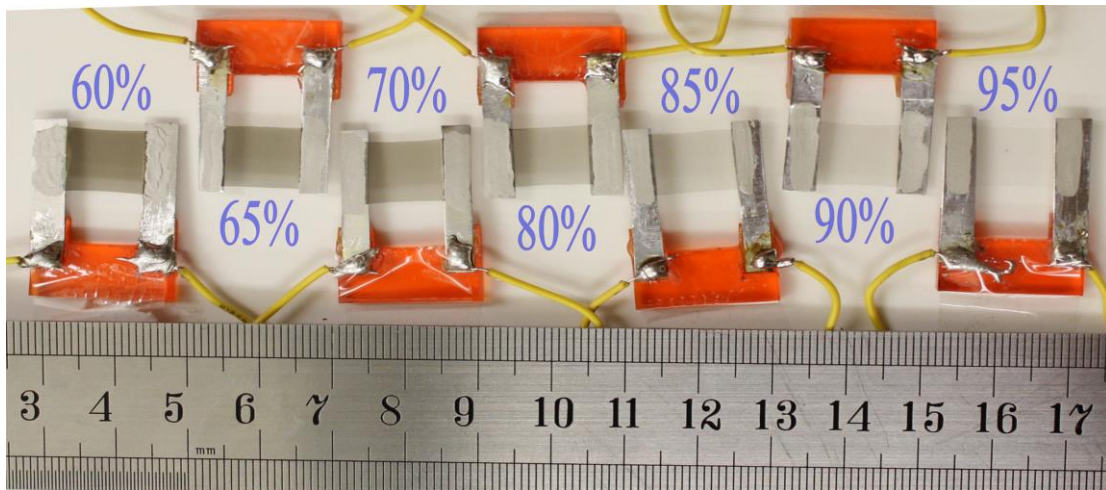


Figure 4.3-1. Freestanding samples of $1 \times 1 \text{ cm}^2$ SWCNT-N% films ($N = 95, 90, 85, 80, 70, 65, 60$) named for their optical transmittance at the wavelength of 550 nm.

The main experimental findings are presented in Figure 4.3-2, which shows plots of frequency-dependent sound pressure measured at the point located at the distance of 3 cm from the center of the sample in the direction perpendicular to sample's plane. The plotted data correspond to SWCNTs samples of different HCPUA: larger transmittance listed in percent next to each plot corresponds to smaller thickness and hence smaller

HCPUA. As expected, the sound pressure increases with the decrease of sample's HCPUA. On the basis of Equation 4.1-23, one can define the so-called "ultimate limit" for the thermophone sound pressure, which corresponds to zero HCPUA ($C_s = 0$). The ultimate limit defines the maximum sound pressure in the process under fixed experimental conditions. Having said that the thermophones sound pressure obtained experimentally is closer to ultimate limit at low frequencies than that at high frequencies. The result is consistent with the Equation 4.1-23 and attributes to the significant increase of $\chi(f)$ at ultrasound frequencies. The ultimate limit and approximations used in derivation of Equation 4.1-23 were tested by direct three dimensional (3D) COMSOL simulations based on coupled Navier-Stocks and Helmholtz equations (Section 4.1.6). Simulations revealed that analytical model discussed in Section 4.1 is accurate and demonstrates the same sound pressure as Equation 4.1-23 in ultimate limit (Figure 4.3-2).

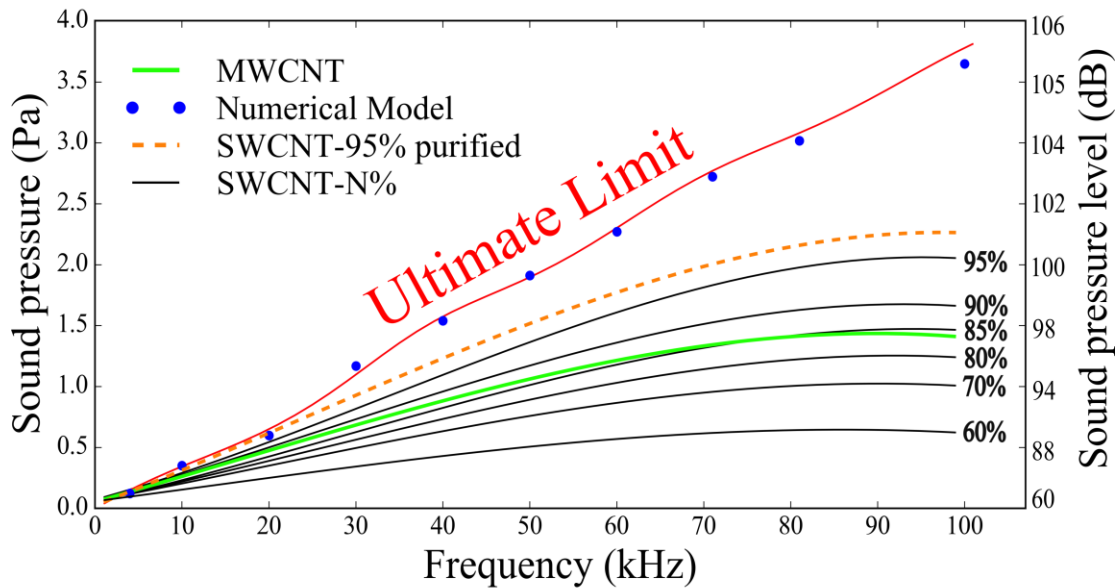


Figure 4.3-2. Sound pressure vs. frequency for various samples normalized to the input power of 1 W. Black lines: averaged curves for SWCNT-N% (N = 60, 70, 80, 85, 90, 95) samples. Orange line: purified SWCNT-95% sample. Green line: MWCNT sample. Red line: the “ultimate” theoretical limit (defined by Equation 4.1-23 with $C_h = 0, r = 3 \text{ cm}, \varphi = 0$ and $\theta = 0$). Blue points: 3D numerical COMSOL modeling (see Section 4.1.6).

To compare SWCNT films performance as thermophone with other materials we performed normalization of literature data to the measurements distance of 3 cm and the input power of 1W. The highest pressure was obtained for the sample SWCNT-95, purified from metallic impurities (see purification method in Section 4.1.5), which demonstrated 2 times higher sound pressure than the closest competitor – MWCNT.

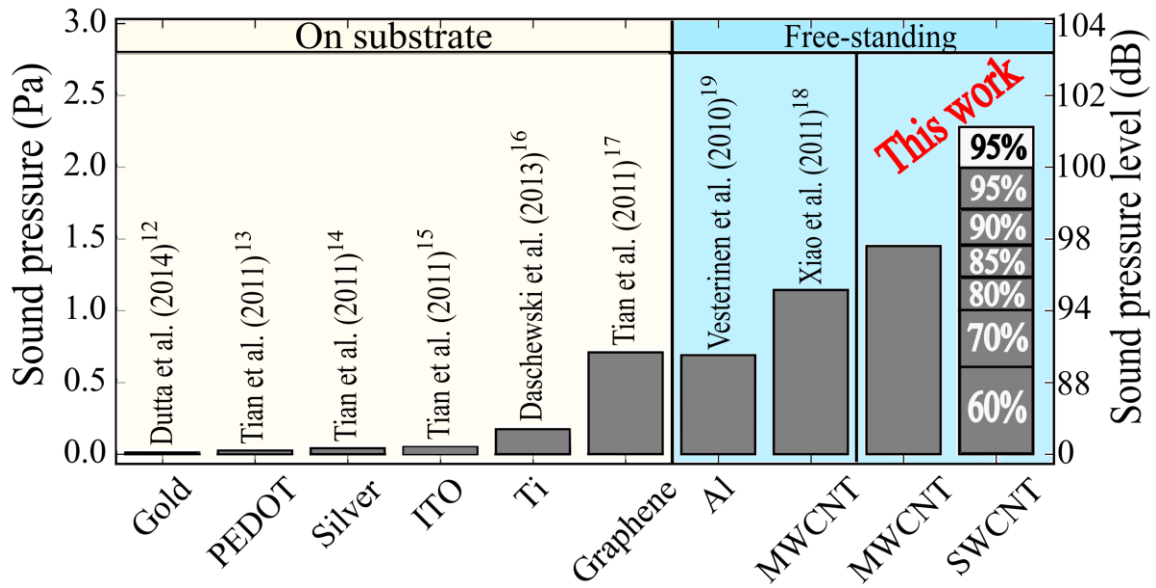


Figure 4.3-3. Reported experimental sound pressure level for various thermophone materials at 100 kHz. The results are normalized to the measurements distance of 3 cm and the input power of 1 W. This work corresponds to the free-standing MWCNTs and SWCNTs samples of different transmittance.

The volumetric effect takes place in thick films and lead to increase of sound pressure (see Section 4.1.5). To demonstrate the effect of volume on the themophone performance in the aerogel structures, we compared surface themophones based on SWCNT films with volumetric themophone from freestanding films of aligned MWCNTs, which were synthesized by a catalytic CVD method in the form of forests⁹⁷. In spite of having different values of HCPUA, the samples SWCNT-85% ($h \approx 60 \text{ nm}$, $C_s = 9.3 \cdot 10^{-3} \text{ J/m}^2\text{K}$) and MWCNTs ($T_{550} = 82\%$, $h \approx 18 \mu\text{m}$, $C_s = 19.4 \cdot 10^{-3} \text{ J/m}^2\text{K}$)⁹⁷ demonstrated similar sound pressure level (Figure 4.3-2), due to volumetric effect in the

MWCNT film. In the experiment conditions, the volumetric effect takes place at thickness over $1 \mu\text{m}$ (see Figure 4.1-6). Hence, MWCNT films with thickness of $\sim 18 \mu\text{m}$ obtain advanced performance due to volumetric effect, whereas SWCNT films with maximum thickness of $\sim 200 \text{nm}$ do not exhibit the effect. Therefore, the SWCNT-85 and MWCNTs samples reach similar sound pressure in spite of higher heat capacity of the MWCNTs.

We now demonstrate that thermoacoustic measurements can be used as an indirect method to obtain the HCPUA and, in some cases, the areal density of materials. In order to do this, we compare measured and predicted by Equation 4.1-23 sound pressures, with the HCPUA as the only undefined parameter. For the free-standing SWCNT films, the HCPUA values were found from the least-squares fitting of Equation 4.1-23 to the sound pressure vs. frequency dependencies using HCPUA as the only fitting parameter. The fitted HCPUA values were then compared with those obtained directly from the measurements of areal density with the help of Equation 4.3-1. The fitted and measured values of HCPUA were found to be in a very good agreement (see Figure 4.3-4a). This method of obtaining HCPUA can be particularly useful, when direct weighing is not possible because of the equipment sensitivity. The performance of purified from iron catalyst particles SWCNT films was also measured, and then, the fitting procedure was repeated for the purified samples (see Figure 4.3-4a and Section 4.4.1). We found that overall HCPUA was indeed reduced by purification, which improved the performance of the SWCNT thermophones.

Another way to assess the results presented in Figure 4.3-2 is to look at the efficiency of the measured thermophones. The absolute efficiency of the thermophones is

defined as the ratio of the average output acoustic power, P_a , to the average applied electric power, P_0 ¹⁹:

$$\eta \equiv \frac{P_a}{P_0} = \frac{4\pi r^2}{P_0 \rho v_s} \int_0^{2\pi} \int_0^\pi p_{rms}^2(r, f, \varphi, \theta) d\varphi d\theta, \quad 4.3-2$$

Our samples under the alternating current heating have low absolute efficiency of around 10^{-6} at 1W of input power. To compare different samples, we calculated the absolute efficiency in the ultimate limit (p_{rms} taken at $C_s = 0$), η_{lim} , and then normalized the experimental values of the efficiency η to η_{lim} . The result for the best performing purified SWCNT-95% sample is plotted in Figure 4.3-4. Even in this case, the ratio η/η_{lim} drops from almost 100% at 1 kHz to 35% at 100 kHz due to the heat accumulation near the sample surface described by $\chi(f)$ in Equation 4.1-23. We estimated from the Equation 4.3-2 that, in order to achieve a relative efficiency of 99% in the frequency range from 1 kHz to 100 kHz under conditions of our experiment, the thermophone active material should have HCPUA equal to $0.4 \cdot 10^{-3} (\text{J/m}^2\text{K})$. Also heat accumulation plays a stronger role in the case of suspended thermophone over a substrate with a small gap. A comprehensive analytical model which covers the point thermophone over such a gaped structure was developed in ¹⁹.

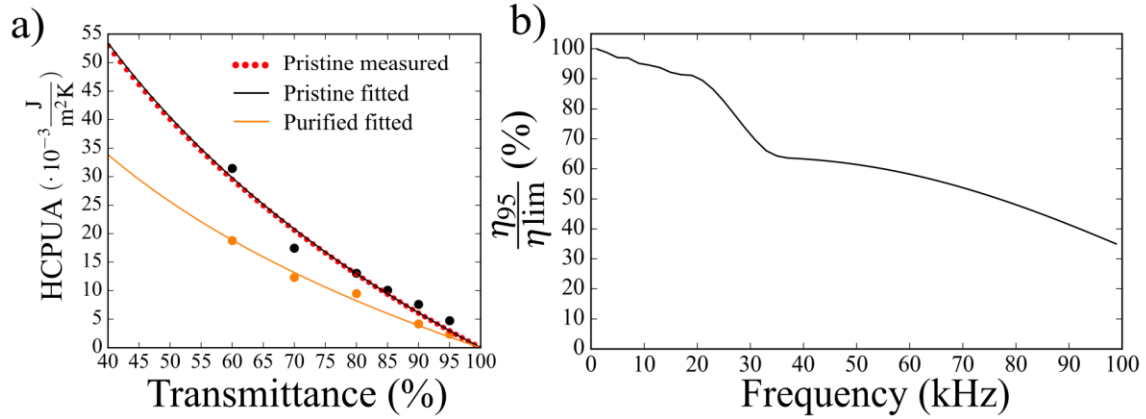


Figure 4.3-4. a) Dependence of HCPUA on transmittance for pristine and purified films. Red dots present HCPUA of pristine SWCNT films measured using areal density from Equation 4.3-1. Black and orange dots present HCPUA for pristine and purified films respectively, which were found from fitting of Equation 4.1-23 to the measured sound pressure vs. frequency. b) The absolute efficiency of the thermophone based on purified SWCNT-95% sample normalized to the efficiency in the theoretical limit (Equation 4.3-2).

4.3.2 Acoustic field anisotropy and diffraction correction

The intensity gain function $G(r, \varphi, \theta)$ defined by Equation 4.1-20 describes the modulation of the sound intensity due to diffraction, which lead to anisotropy of the sound pressure. We computed $G(r, \varphi, \theta)$ using Huygens-Fresnel principle (see Section 4.1.4). In order to measure anisotropy, we placed the purified SWCNT-95% sample on a stepper motor and rotated it with respect to the microphone, changing the angle, θ , in the range of $[0, 2\pi]$, while the sound frequency was fixed at 6, 32, 40, or 64 kHz (Figure 4.3-5). At 6 kHz, we detected nearly isotropic pressure distribution associated with a point-like sound source. At frequencies of 32, 40 and 64 kHz, we observed a transition from the isotropic point-source regime to the anisotropic regime caused by the finite size of the source in

terms of the sound wavelength. In the latter regime, the natural diffraction focusing appears in both sides of the sample for $\theta = 0^\circ$ and 180° . The transition between the regimes is defined by geometric parameters of the system. In our experimental setting, the wavelength varies from $\lambda = 0.34$ cm (at 100 kHz) to 34.3 cm (at 1 kHz), while the sample size and the distance to the microphone are fixed to 1 cm x 1 cm and $r = 3$ cm, respectively. Obtained sound pressure distributions prove an importance of diffraction corrections in theoretical description of thermophones at high frequencies.

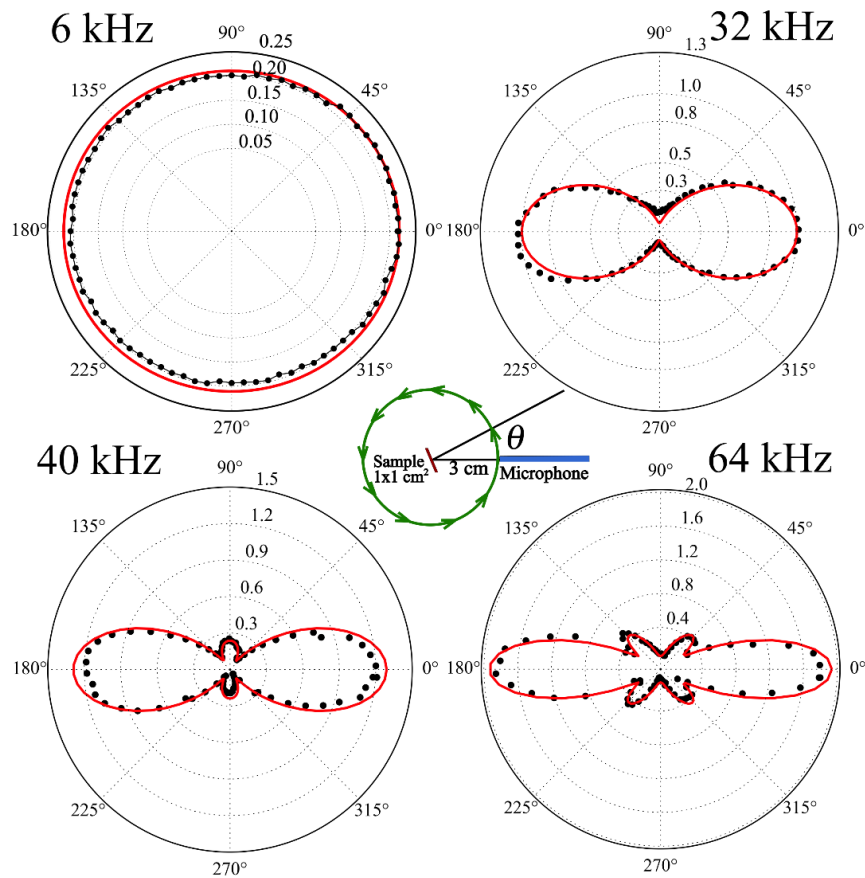


Figure 4.3-5. Sound pressure, measured in pascals, dependence of purified SWCNT-95 on azimuthal angle, $\theta \in [0, 2\pi]$, for frequencies: 6, 32, 40 and 64 kHz. Red lines represent the

theoretical limit calculated from the Equation 4.1-23 black dots represent experimental data.
Measurements were normalized to the input power of 1 W at the distance of 3 cm.

4.4 Increasing the performance of SWCNT films

To the best of our knowledge, thermophones based on the SWCNT films demonstrate the highest efficiency among all the materials as presented in Section 4.3. Achieved efficiency in the frequency range of 1-100 kHz is close to the ultimate limit of the thermophones (Figure 4.3-4). However, the ultimate limit depends on the conditions of an experiment: room temperature, air media, natural convection, current signal shape *etc.* Changes in the conditions allow to approach an increase of thermophones performance. For instance, switching the surrounding media from air to one with lower specific heat capacity such as Ar or Xe^{85,98} or decreasing its temperature increases the ultimate limit in accordance with the Equation 4.1-23.

This section introduces modifications of material structure, device fabrication and conditions of operation to increase the thermophones performance. From the discussion in Section 4.3.1 it is evident that purification of SWCNT films from catalyst nanoparticles reveals in advanced characteristics of the thermophones. Comprehensive investigation of the purification process by Joule heating in vacuum governed in Section 4.4.1. Problem of carbon nanotube oxidation in air raise when thermophone operates at high temperatures. The problem is addressed in Section 4.4.2 where covering of the CNTs with a thin layer of Al₂O₃ leads to an advance performance of thermophones and protect from CNTs oxidation. In addition, encapsulation of CNT films into the closed system filled with inert gas introduces a device with protection from oxidation. The modification concerning conditions of operation rely on switching from sinus signal to pulse signal with small duty

cycle towards increase of thermophones efficiency. The investigation is covered in Section 4.4.3 and opens new perspectives. Indeed, the method leads to 7 folds increase in efficiency of thermophones being applied to devices encapsulated in inert gas.

4.4.1 Joule assisted purification and its effect on thermophones efficiency

Typically high temperature annealing for illumination of nanoparticles performs in furnaces and leads to evaporation of metals (>1500 °C), while maintaining nanotube morphology, and even removes defects⁹⁹. This approach requires high-temperature equipment and high energy investment, in addition to high vacuum or extremely pure gases to prevent nanotube oxidation^{100,101}.

Here, we propose a simple and elegant method of high temperature SWCNT purification from catalyst residuals by Joule heating in vacuum conditions. The developed method of the Joule-assisted purification is energy-efficient, local, fast, and scalable. To examine the kinetics of the iron particle elimination, we carried out *in situ* and *ex situ* transmission electron microscopy (TEM) studies coupled with numerical simulations of SWCNT film heating and Fe evaporation. Correspondingly, UV-Vis-NIR and Raman spectroscopies coupled with 4-probe resistance measurements provide a comprehensive insight into the evolution of SWCNT film characteristics after purification. Then, we examine the influence of the purification on the performance of SWCNT films as air-coupled thermophones.

SWCNT films utilized in this work contain metallic impurities either in the form of active catalyst particles inside SWCNTs or iron particle residuals on the surface. Figure

4.4-1a,b illustrates typical TEM images of the SWCNT-90 films before and after the Joule-assisted purification: Fe particles disappear, while the general morphology of nanotubes remains almost the same.

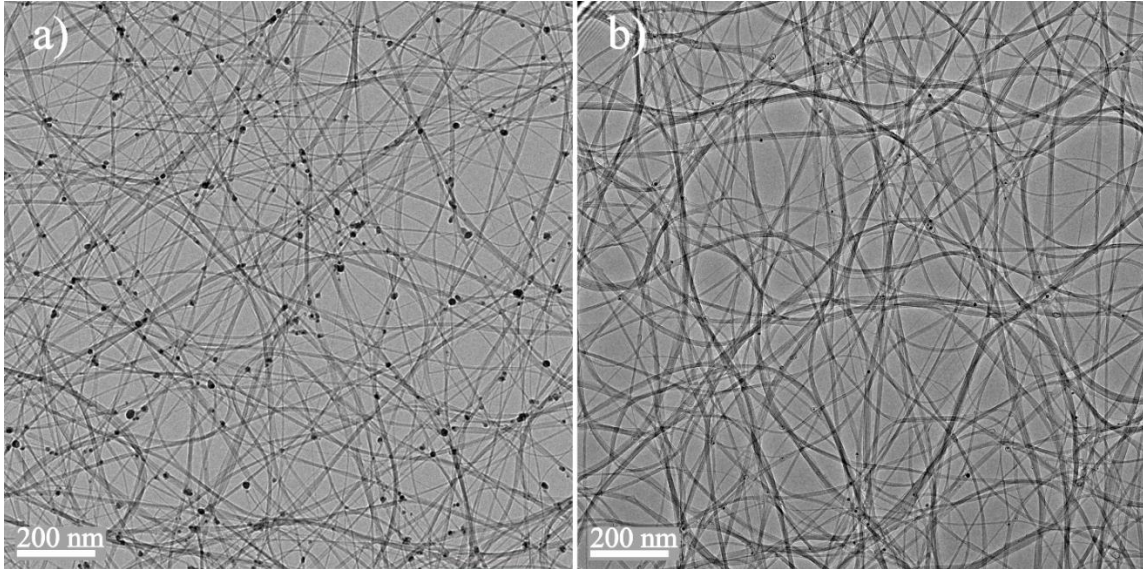


Figure 4.4-1. Typical TEM images of a) pristine and b) purified (2 min at 1600 °C) SWCNT films. The contrast black dots correspond to the iron nanoparticles.

From theoretical point of view, there are two types of solid to gas phase transitions: direct sublimation and indirect evaporation via an intermediate liquid step. The rates of both Fe evaporation or sublimation can be described by the modified Hertz-Knudsen equation¹⁰²:

$$\frac{dr}{dt} = \frac{a_c(P_m - P_p)}{\rho_p \sqrt{2\pi RT/M}} \quad 4.4-1$$

where r is the particle radius, a_c is the accommodation coefficient, P_p and P_m are respectively the partial vapor pressures of iron over the particle and within the media, ρ_p

is the density of an iron particle, R is the universal gas constant, T is the particle temperature, M is the iron molar mass. Due to the size-effect, smaller Fe nanoparticles in the SWCNT films ought to evaporate faster. The partial vapor pressure above the curved surface is much higher than that for the bulk and depends on the particle radius, r , according to the Kelvin equation:

$$P_p = P_\infty \exp\left(\frac{2\gamma_f V_m}{rRT}\right), \quad 4.4-2$$

where P_∞ is the equilibrium vapor pressure for bulk, γ_f is the surface tension, V_m is the molar volume. Dependency of the partial vapor pressure on the particle radius (the Kelvin effect) dramatically influences the rate of nanoparticle evaporation (Figure 4.4-2a). Taking into consideration the Kelvin effect, the integration of equation 4.4-1 results in a temperature dependence of the evaporation time for Fe nanoparticles of sizes 1 – 25 nm (see Figure 4.4-2b). The majority of nanoparticles in the SWCNT films are smaller than 25 nm and, according to the theoretical evaluation, should evaporate in 1 h at 1000 °C or in 2 min at 1200 °C.

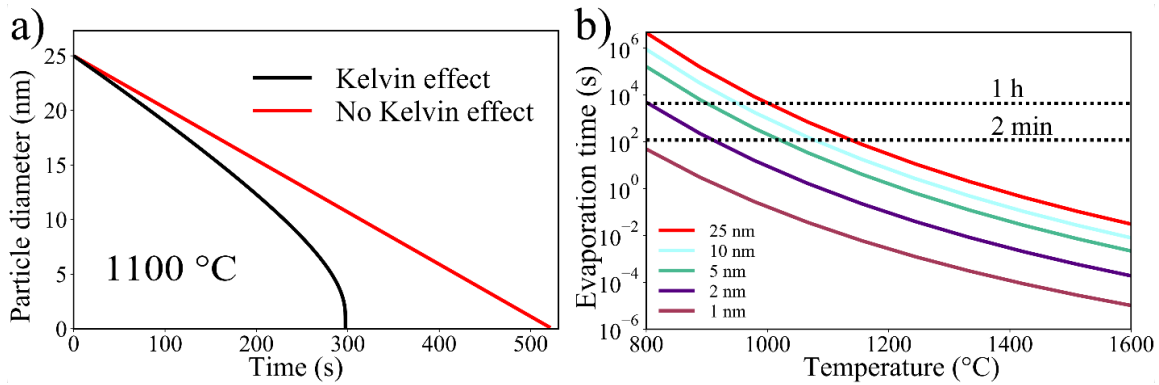


Figure 4.4-2. a) Time evolution of nanoparticle diameter at 1100 °C: the black line is calculated assuming the Kelvin effect (Equation 4.4-2), the red line is obtained without the Kelvin effect assuming that the equilibrium pressure over nanoparticles does not depend on the particle radius, i.e. $P_p = P_\infty$. b) Dependence of evaporation time on the temperature for nanoparticles with different diameters. Dashed lines correspond to heating time of 2 min and 1 h.

To provide the fine control of temperature on the surface of SWCNT films by Joule heating, we measured the dependence of temperature on an input electrical power and supported the experimental results numerically (see Section 4.2). Figure 4.4-3 represents the evolution of the iron nanoparticles during the Joule-assisted purification by means of *ex situ* TEM imaging. To achieve the rapid cleaning of nanotubes from catalyst particles, we fixed the treatment time to be 2 min and varied the temperature in the range of 800 – 1600 °C. According to the experimental results, the majority of particles vanishes at 1600 °C (Figure 4.4-3a), unlike in the abovementioned theoretical prediction of 1200 °C (Figure 4.4-2b). It is worth noting that some particles with a large diameter of ~16 nm evaporate at 1200 °C (red marks). The comparison of theoretically predicted and experimentally measured particle size distributions implies the existence of additional parameters influencing the evaporation rate, which however were not included in the model. Indeed,

at higher temperatures the theoretically predicted particle distributions shift towards the smaller diameters, unlike the experimentally measured ones (Figure 4.4-3b). Moreover, *in situ* TEM heating experiments revealed different evaporation rates for particles of similar diameters (Table 4.4-1¹⁰³). Among different effects, we attribute this experimentally observed difference in evaporation rate to the following facts: i) during the evaporation the particle composition changes due to carbon solubility in iron and possible phase transition of Fe-C alloy into cementite Fe_3C^{71} , which lowers the equilibrium vapor pressure over the particle; ii) the iron partial pressure above the particle inside the restricted carbon shell volume remains higher than outside, which also hinders the iron evaporation.

Table 4.4-1. Different evaporation rate of iron nanoparticles with similar diameters defined from *in situ* TEM experiments at 1000 °C ¹⁰³.

	Group of evaporated particles	Group of not evaporated particles
Mean diameter (nm)	9	7
Evaporation rate (nm/s)	0.02	0.11

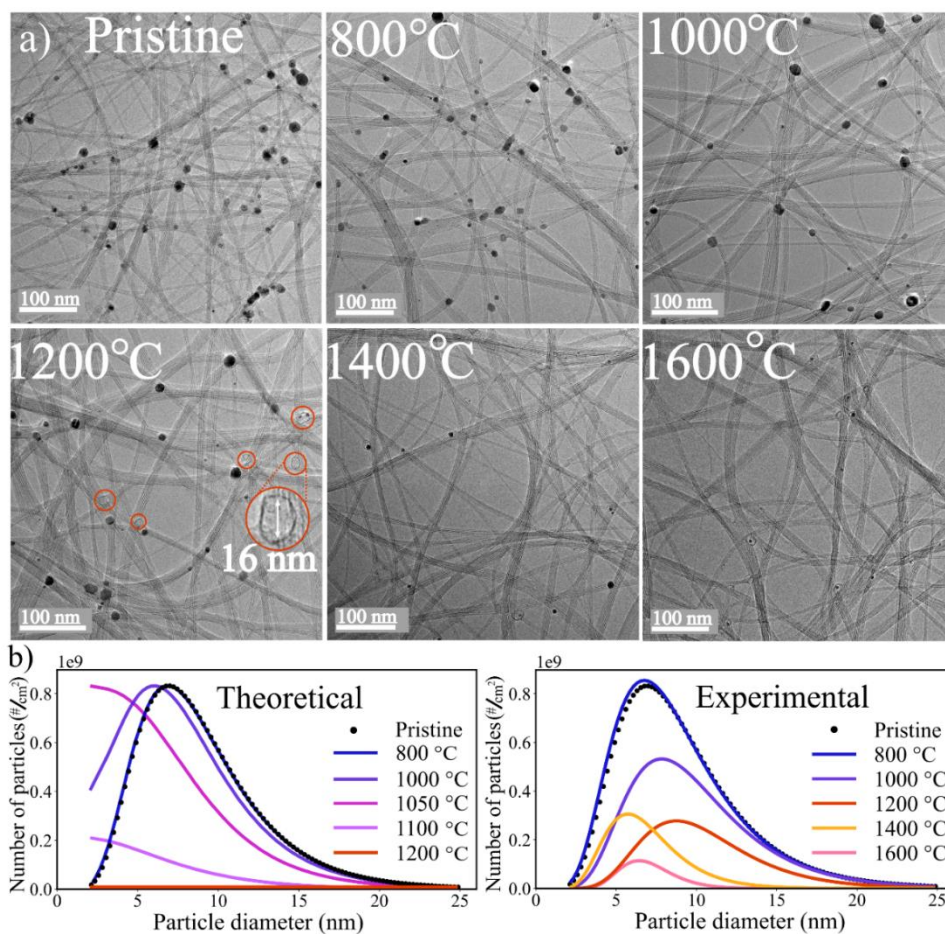


Figure 4.4-3. a) Typical *ex situ* TEM images of SWCNT films after 2 min treatment in the temperature range from 800°C to 1600°C. b) Theoretically and experimentally obtained evolution of nanoparticle distribution after 2 min of purification.

To characterize the amount of evaporated particles, we used the areal density of iron nanoparticles in SWCNT films based on TEM statistics over an average area of at least 4 μm^2 for each temperature (Figure 4.4-4). The resulted iron areal density for the pristine SWCNT film ($\rho_a=110 \text{ ng/cm}^2$) turned to be in a good agreement with the direct weighing of the similar films ($\rho_a=187 \text{ ng/cm}^2$) defined by Equation 4.3-1, thereby, validating the approach. The correct areal density should lay between these two values.

Indeed, a TEM image is a contrast- and focus-dependent method leading to an underestimated value; while weighing method overestimates the correct value, being arranged for a thick SWCNT film and recalculated for thin films assuming a homogeneous iron distribution over the thickness. The 2 min purification at 1600 °C results in the iron areal density of $\rho_a=4 \text{ ng/cm}^2$, which is 27 times less than those for the pristine film (Figure 4.4-4). Assuming the iron content of 17% as in the pristine thick films from weighing experiment⁹⁶, it turns to 0.6% for the treated sample. The value also agrees with the results of energy-dispersive X-ray spectroscopy (EDX) measurements performed in TEM (0.4 wt.%). Thus, the high temperature Joule heating in vacuum provides a simple and fast route for the purification of SWCNT films.

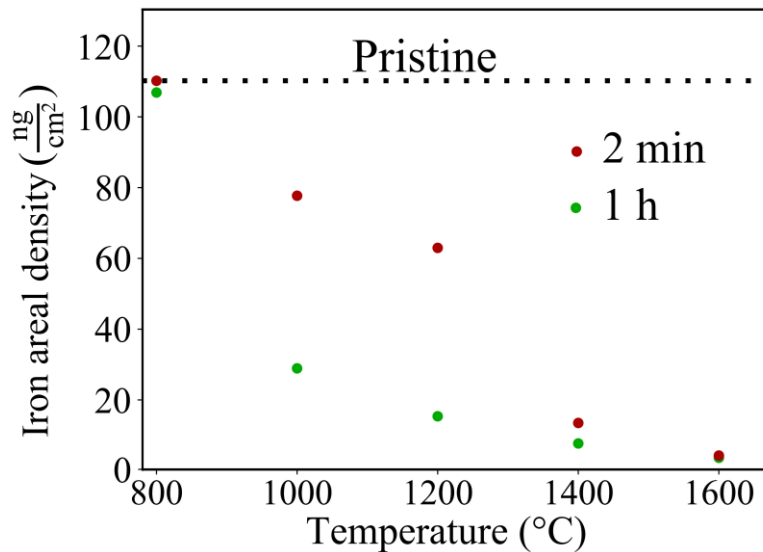


Figure 4.4-4. The dependence of iron areal density calculated from TEM images on the purification temperature for 2 min and 1 h of Joule heating.

Initially, the SWCNT films contain iron nanoparticles encapsulated in carbon shells (Figure 4.4-5a). The Joule-assisted purification of SWCNT films in many cases removes only the iron core, while the carbon shells remain almost intact (Figure 4.4-5b). Nevertheless, the annealing introduces new defects resulting in a decreased ratio of the intensities of G to D modes (I_G/I_D) in a Raman spectrum (Figure 4.4-6a). The bell-shaped dependence of I_G/I_D can be attributed to two competing processes at high temperatures: iron evaporation and carbon solubility. At temperatures below 1200 °C, the process of carbon solubility is fast enough to increase the number of defects. Whereas, at higher temperature (>1200 °C) the evaporation process dominates resulting in a lower level of defects. In other words, the faster the iron evaporation the lower the number of defects. In our experiments, the fast treatment at 1600 °C resulted in $I_G/I_D = 180$, which insignificantly differs from the initial value of 224.

The sheet resistance of SWCNT films is one of the most important parameters indicating the quality of carbon nanotubes. The sheet resistance of treated SWCNT films is highly dependent on the residence time in the atmosphere after processing, because of the doping by surrounding atmosphere¹⁰⁴. To provide reproducible resistance values, we performed the measurements in a week after the purification, storing the sample at ambient conditions (Figure 4.4-6b). The obtained results for sheet resistance values correlate well with the defectiveness, demonstrating lower resistance for SWCNT films with a higher I_G/I_D ratio (Figure 4.4-6a)¹⁰⁵. To verify the data we arranged the films doping with the solution of H₂AuCl₄ in ethanol (Figure 4.4-6b). The results indicate the similar curve

behavior for pristine and doped SWCNT films, except the different values for initial and treated at 1600 °C films, which in the case of doped films give the same value (51 Ohm/sq), unlike those for pristine. The similar resistance for doped films achieved because of the low level of defects in SWCNT films after processing at 1600 °C. Whereas we assume the mismatch in pristine samples caused by different levels of penetration of surrounding molecules from the gas phase into the bundle of SWCNTs network, thereby indicating a more compact structure of bundles after high temperature annealing. The problem of penetration was overcome by the liquid solution of H₂AuCl₄ in ethanol.

The heat treatment of the SWCNT films revealed an insignificant effect on optical spectra: the difference in transmittance of annealed (for 2 min at 1600 °C) and pristine films achieves no more than 1% at the wavelength of 274 nm, while in the visible range it is as low as 0.2% (Figure 4.4-6c). The negligible difference implies that the complex background of the optical spectrum (usually attributed to carbon π -plasmon and metal impurities) is mostly due to the carbon species. Thus, according to optical, Raman and electrical measurements, the thermal purification unveils almost no harm to the optical properties of SWCNT films.

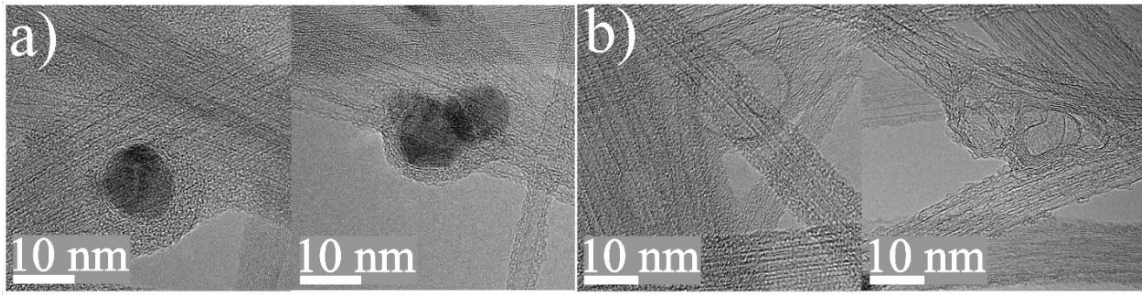


Figure 4.4-5. TEM images of typical a) iron nanoparticles in carbon shells and b) carbon shells that remain after the iron evaporation.

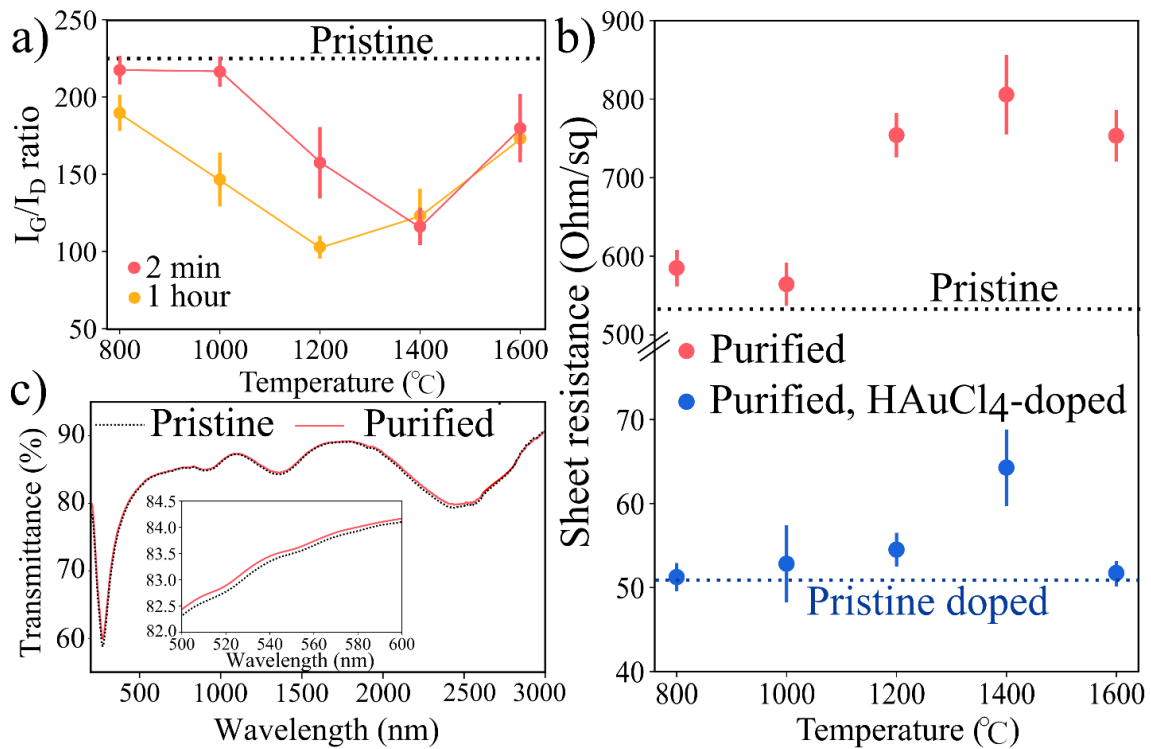


Figure 4.4-6. a) The dependence of the I_G/I_D intensity ratio in Raman spectra on the temperature of treatment during 2 min and 1 h treatment time. The dashed black line corresponds to I_G/I_D ratio of the untreated pristine sample. b) The dependence of the sheet resistance on the treatment temperature (for 2 min) of purified samples and purified samples doped with HAuCl₄. The dashed black and blue lines correspond to pristine and untreated doped samples, respectively. c) The spectral dependence of transmittance of the pristine SWCNT film (dashed black line) and the sample annealed at 1600 $^{\circ}\text{C}$ for 2 min (red line).

Temperature treatment by Joule purification of SWCNTs samples reveals an increase of the sound pressure after the purification, because of the decrease in the areal density. The level of the increase of the sound pressure is frequency dependent as expected for materials with initially low heat capacity in accordance to Equation 4.1-23 (Figure 4.4-7). In the case of our SWCNT films, the iron-free samples demonstrate in average 24% higher sound pressure for the frequency range from 80 to 100 kHz.

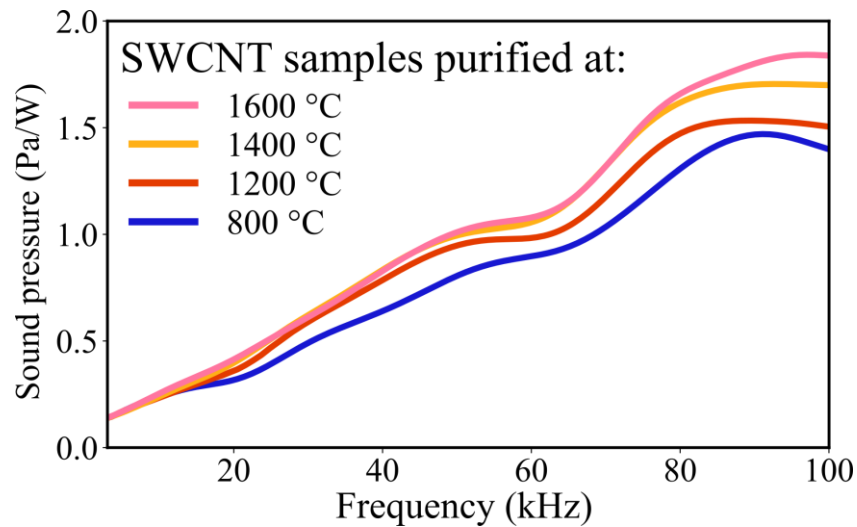


Figure 4.4-7. The frequency dependence of the sound pressure generated by free-standing SWCNTs samples treated by Joule-assisted purification at different temperatures for 2 min.

4.4.2 Environment protected thermophones

SWCNT films along with numerous of advantages for thermophones applications such as easy samples handling, highest sound pressure, superior synthesis process etc. have a few limitations. The performance of the films is influenced by the surrounding media. At high temperatures SWCNTs oxidize in the presence of oxygen. Typical temperatures for

the oxidation of SWCNT films under impact of Joule heating is 350-450 °C, which corresponds to the input power density of 1.5-2.0 W/cm² (Figure 4.2-3). Therefore, the limitation of the input power density restricts the maximum sound pressure of thermophones operating in harsh environments.

To overcome the problem of the SWCNTs oxidation at high temperatures a deposition of nanometric layer of Al₂O₃ on top of the SWCNTs was utilized (Figure 4.4-8a). The coverage was performed by atomic layer deposition method^{106,25}. There are two competing factors, which define the optimal coverage thickness. On the one hand, the HCPUA of the thermophone increases with the Al₂O₃ thickness, which decrease an efficiency of themophones. On the other hand, the Al₂O₃ protection lead to increase of the input power and allows to operate thermophones at higher temperatures without an oxidization to take place. Therefore, the technical task was to protect SWCNT films with thinnest possible covering layer. Empirically it was determined that the coverage of SWCNTs with 5 nm layer of Al₂O₃ results in maximum power density of 6.8 W/cm² and demonstrate 70% increase of the maximum sound pressure (Figure 4.4-8b).

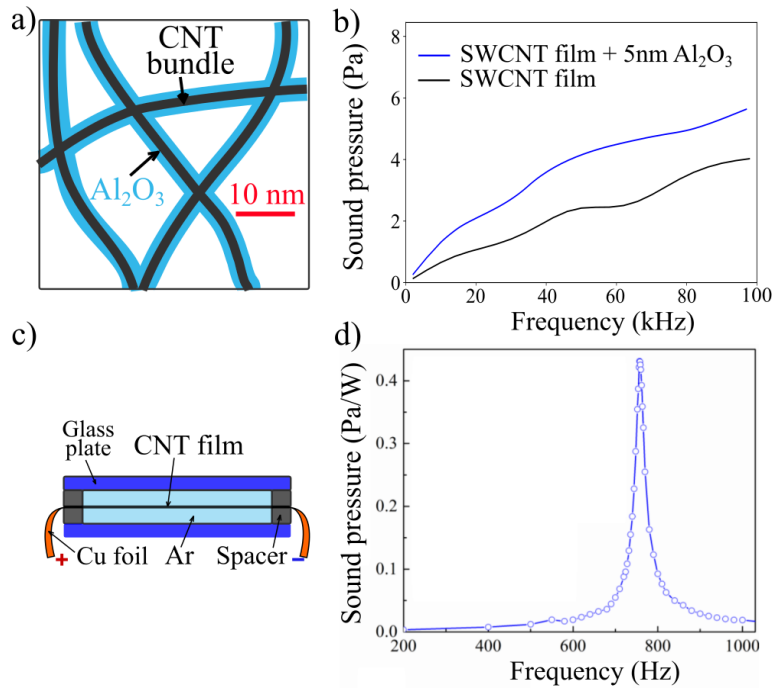


Figure 4.4-8. a) Schematic illustration of SWCNTs covered with nanometric layer of Al₂O₃. b) The dependence of maximum sound pressure on frequencies for pristine film (black line) and covered with 5 nm layer of Al₂O₃ (blue line). c) Schematic illustration of CNTs encapsulation into atmosphere of Ar. d) Typical resonance response of encapsulated thermophone based on CNTs.

Protection of CNTs from oxidization is achievable by their encapsulation into atmosphere of inert gases^{85,107} (Figure 4.4-8c). Such encapsulation introduces corrections to the sound pressure and introduces mechanical vibrations of the covering membranes. Consequently, the amplitude frequency response and sound propagation from encapsulated device (closed system) defines by the covering membranes resonances. The sound pressure for the encapsulated system was derived by Arnold and Crandall⁶³

$$p_{rms} = \frac{(1 - \gamma)P_0}{\sqrt{2}\pi fV}, \quad 4.4-3$$

where γ is the heat capacity ratio of air and V is the volume inside the encapsulated system. According to the Equation 4.4-3 to produce high sound pressure one should tend to decrease the volume of encapsulated device and utilize low frequencies. The mechanism of sound generation of closed system relies on the heating of the CNTs which leads to gas expansion and forces the covering membrane to vibrate and excite the sound propagation¹⁰⁸. Now the thermophones amplitude frequency response is hosted by resonances of the covering membrane and governed by dimensions of the device^{63,85}. For instance, in the case of device size 11.9 x 17.0 x 0.2 cm³ the resonance frequency is 750 Hz (Figure 4.4-8d). To maximize the sound pressure, the excitation frequencies should match self-modes of membrane vibrations or their harmonics. The principle advantage of encapsulated thermophones over opened is inert gas media surround the sample, which allow to increase the input power from a few to dozens of watts without CNTs oxidization. For encapsulated thermophones the efficiency significantly increases from 10⁻⁷ (opened system, P₀=1W) to 1% (closed system, P₀=65W), because now larger input powers are applicable¹⁰⁷.

4.4.3 Pulse induced sound generation

The rectangular single pulse (SP) signal with low duty cycle (D_s) was employed to improve heat dissipation from the thermophone and increase the sound pressure (Figure 4.4-9a). Under impact of SP signal sample heats for the period of time $t_h = D_s/f$ and for the rest time $t_c = (1 - D_s)/f$ it cools. This type of signal provides sufficient time for the

samples to reach a background temperature level after heating, therefore increasing efficiency of sound generation.

As was mentioned in Section 4.1.2 the temperature variation in time is essential to produce thermal expansion and sound propagation. For sine signal excitation there are two components of power (Equation 4.1-1). The large amount of constant in time power, P_0 , heats the sample to the constant in time temperature, T_{avg} , which results in no sound generation and waste of energy (see Figure 4.1-2). Whereas, for SP signal the temperature oscillations start from the background level and turn back to the same background level. Therefore, the applied power introduces higher time derivative of temperature, which results in the efficiency increase. However, the combination of excitation period and duty cycle has to be long enough to provide cooling and to produce change of temperature in time.

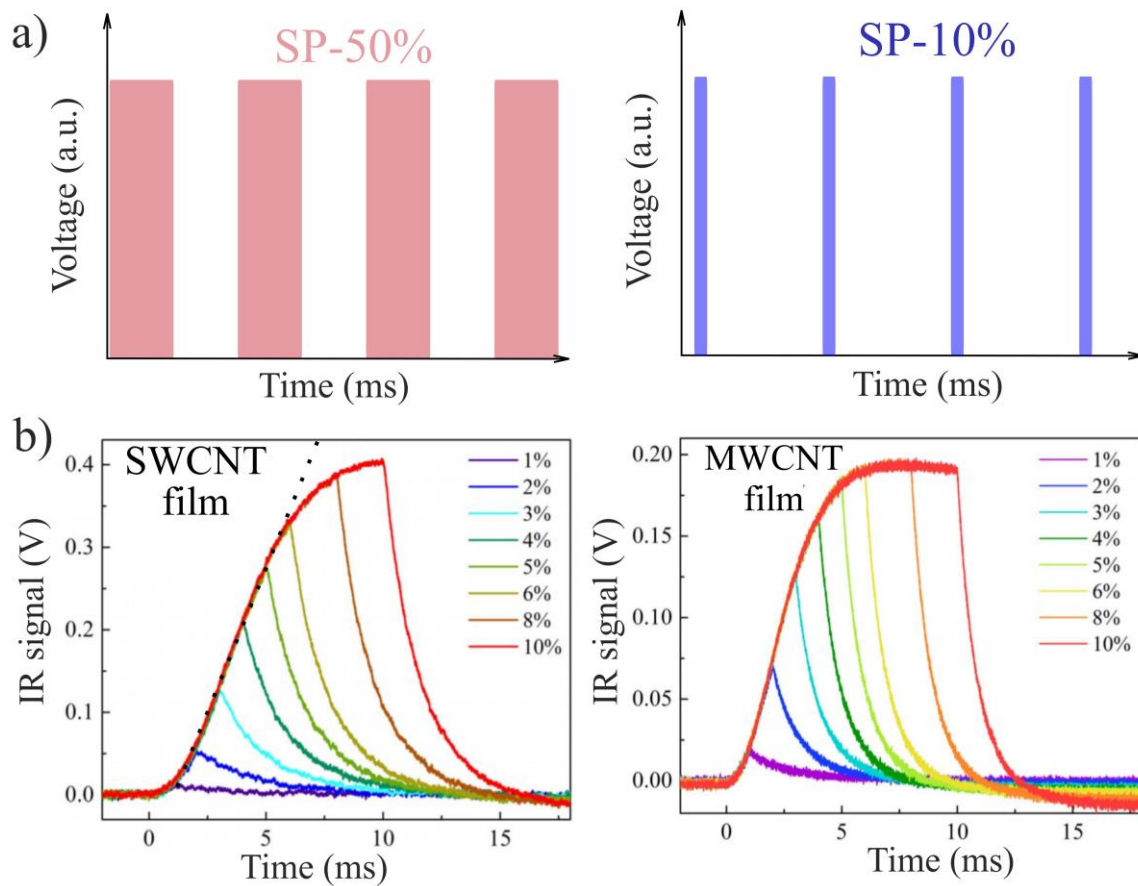


Figure 4.4-9. a) Schematic representation of rectangular single pulse signal with duty cycles of 10% and 50%. b) Received blackbody radiation signal for increasing duty cycles in the range 1-10% from MWCNT and SWCNT films placed in vacuum.

To estimate optimal duty cycles of SP signal, a vacuum measurements were employed. The SWCNT-85 sample was placed into vacuum chamber and heated by Joule heating, while the IR detector measured the radiation power. From the dependence of radiation power on time one can conclude that duty cycles below 6% perfectly fits for efficient heating (Figure 4.4-9b). For larger duty cycles, the signal losses linear time dependence and slopes to constant value, which results in no sound generation as was

mention above. Therefore, the signals with small duty cycles were considered in this section. Moreover, the radiation power is a function of the sample temperature and allows estimating HCPUA:

$$C_s = \frac{P_0}{S \frac{dT}{dt}} \quad 4.4-4$$

From comparison of MWCNTs and SWCNT-85 one can see larger slope of signal for SWCNT-85 sample, which means its smaller HCPUA (Figure 4.4-9b). In combination with the fact of similar sound pressure for those two samples observed in Section 4.3.1 this once again confirms volumetric effect in MWCNT.

Utilization of SP signal with 1-10% of duty cycle leads to increase of sound pressure in thermophones. The efficiency increased 1.8 times compared to sinus signal generation (Figure 4.4-10). In the case of longer duty cycles, the heat accumulation takes place and decrease the efficiency¹⁰⁷.

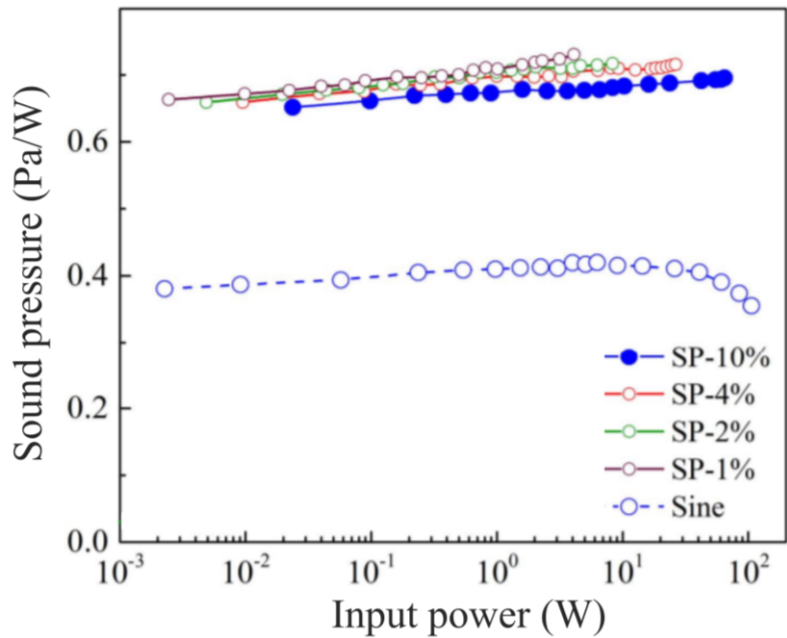


Figure 4.4-10. The sound pressure versus input power for the excitation with SP and sine signals at frequency of 750 Hz.

4.5 Application of thermophones

To propose an application to a new technology, one should analyze its advantages along with disadvantages. Being fascinating phenomenon, thermophones have flat amplitude frequency response and wide bandwidth. Other unique properties of the thermophone comes after the utilized conducting material. For instance, thermophones based on flexible, stretchable and transparent materials inherit these properties. Among the problems towards thermophones application dominates two: low efficiency and

irreversibility of thermoacoustic effect in thermophones. However, there are applications which do not require these properties.

One of the possible applications of thermophone based on SWCNT films is a calibrating device for ultrasound equipment. Indeed, such device requires a flat amplitude frequency response and wide bandwidth. Whereas, the device hosts without sound detectors, which means that irreversibility of the thermophones is not an obstacle in this application. Moreover, thermophones has exceptionally large range of surface areas from nm^2 to m^2 , which along with flexibility and stretchability is cutting edge for the systems shapes and further applications in, for instance, phase arrays.

The field of thermophones is novel for practical applications, despite its long history. Therefore, a first patent in the field was issued in 2011 (Figure 4.5-1). To the date, there are about a hundred of related to thermophones patents according to the United States patent and trademark office¹⁰⁹. The vast majority of patents proposes devices such as headphones and loudspeakers, which operate in acoustic range. Only a few patents are related to the ultrasound frequencies.

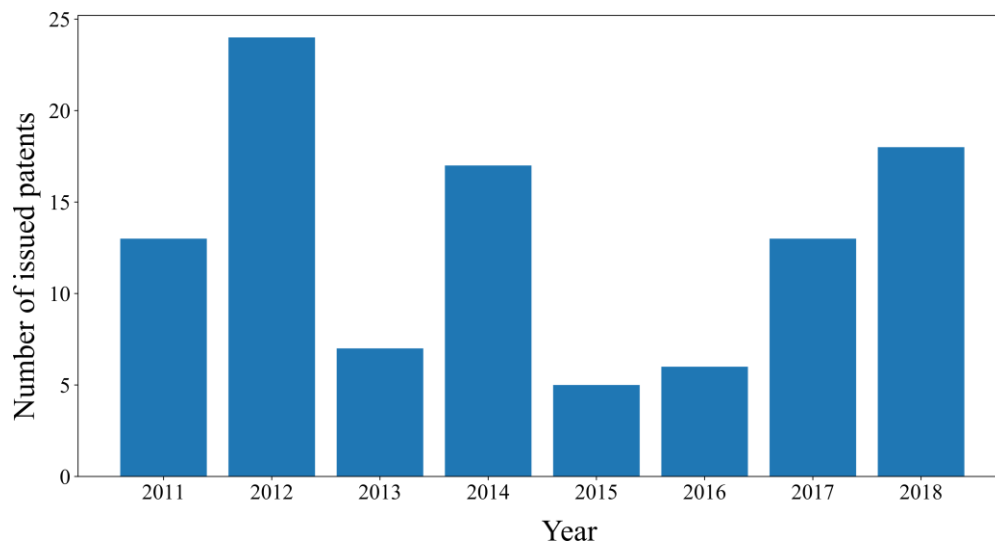


Figure 4.5-1. Number of issued patents on thermophones according to the United States patent and trademark office¹⁰⁹.

The ultrasound positioning systems is a rapidly developing and perspective field^{110,111}. For higher flexibility, the systems require ultrasound antennas with wide directivity function and bandwidth¹¹², *i.e.* sources of sound, which provide isotropic ultrasound propagation in the space with continuous function of frequency. Typically, the positioning systems employs frequencies of 20-40 kHz, for instance in robotics applications. Commercially available ultrasound transducers of these frequencies are based on piezoelectric effect and exploit narrow directivity function in combination with resonances in amplitude frequency response. Therefore, to fulfill the technical needs of positioning application a single ultrasound antenna employs many transducers to provide a wide directivity function, which raises synchronization problems and complicates fabrication. Thermophones directivity functions for rectangular samples is far from wide at ultrasound frequencies (Figure 4.3-5). However, the thermophones being assembled in

cylindrical shape reveals wide directivity function (Figure 4.5-2a,b). The assembling of such antenna is exceptionally simple and carries out by transferring of the SWCNT films on top of the cylindrical surface with pores, which then covers by metals for a contact. The cylindrical shape of the substrate provides the wide directivity at frequency of 40 kHz. Whereas, the pores in substrate increases the sound pressure because of two facts: i) the reflected sound wave from the substrate increase the sound pressure from external side, due to SWCNTs transparency with respect to the gas molecules (Figure 4.5-2c), ii) heat conductivity into the substrate is suppressed for free-standing films over the pores, which increases the efficiency. Overall, thermophones from SWCNT films capture the essential features for the positioning applications as an ultrasound antenna.

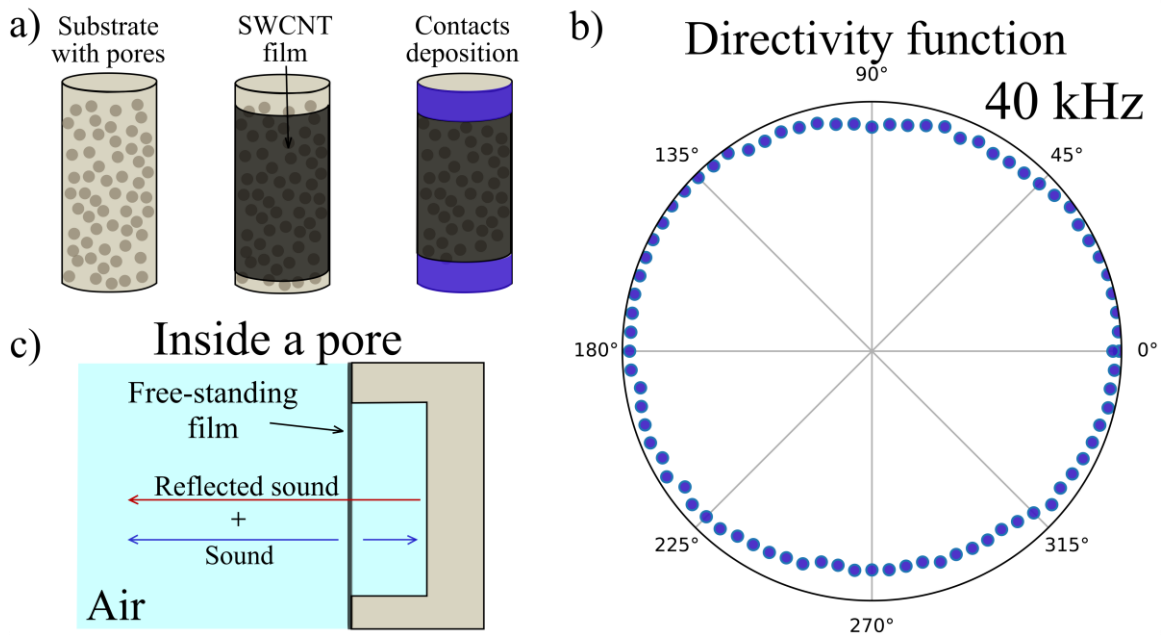


Figure 4.5-2. a) Fabrication process of thermophone wide directivity ultrasound antenna and b) its typical directivity function at 40 kHz. c) The schematic illustration of sound reflection inside a pore of the substrate.

Chapter 5. Conclusions

The SWCNT films demonstrated the state-of-the-art performance as a material for thermophone applications. The extremely low HCPUA of $3.2 \cdot 10^{-3} (\text{J}/\text{m}^2\text{K})$ allowed to achieve record sound pressure and fourfold increase in the efficiency in comparison to other materials utilized in thermophones under the equivalent conditions.

The significant role of acoustic field anisotropy at ultrasound frequencies was demonstrated experimentally. In addition, the theoretical approaches were extended here to analytically consider the anisotropy. Moreover, this thesis demonstrates both theoretically and experimentally the volumetric effect in thermophones to exhibit superior increase of the sound pressure. The results suggest production of sparser aerogel materials to approach the limit of efficiency in thermophones. Also, theoretical estimations predict flat thermophone with HCPUA of $0.4 \cdot 10^{-3} (\text{J}/\text{m}^2\text{K})$ to achieve the ultimate sound pressure limit.

The methods towards modification of the thermophones performance were proposed. Encapsulation of CNT films into atmosphere of inert gas or its covering with nanometric layer of Al_2O_3 overcome oxidization problem of CNT films at high temperature. Both methods lead to increase of maximum sound pressure. Coverage with Al_2O_3 revealed in sound pressure increase of 70%, while keeping the flat amplitude frequency response of the thermophones. Whereas, films encapsulation lead to resonances, but results in exceptional 7 folds increase of the thermophone efficiency. Moreover,

exploiting of the pulse signal instead of sinus signal provides additional 80% to the thermophone efficiency.

The simple, fast, resource-efficient, and universal method of the SWCNT films purification by Joule heating was proposed. The method allowed rapidly decrease the catalyst impurities from SWCNT films at 1600 °C for 2 min without significant damage to the nanotube structure. The Joule-assisted purification resulted in advanced performance of SWCNT films as an active component of thermophones. The proposed method of purification can be easily extended to other applications, for instance, the SWCNTs-based devices of limited liquid and harsh reagent tolerance like nanotube aerogels and drug delivery systems.

There is a number of advantages, which make SWCNT films attractive for thermophone applications compared to other materials. In terms of the sound generation, these advantages are: (i) the highest sound pressure, (ii) low sheet resistance; and in terms of synthesis: (iii) easy sample handling, and (iv) fast, scalable and inexpensive production. The excellent performance of SWCNT film based thermophones opens a new avenue for a number of potential applications. The wide bandwidth and flat amplitude-frequency response of the thermophones can be applied in the devices for calibrations of ultrasound detectors. The possibility to produce themophones from thin SWCNT films, in a flexible shape, and with a large surface area allows to make devices with a wide directivity, which can be used, for instance, in robots positioning applications.

Bibliography

- (1) Kiserud, T.; Piaggio, G.; Carroli, G.; Widmer, M.; Carvalho, J.; Neerup Jensen, L.; Giordano, D.; Cecatti, J. G.; Abdel Aleem, H.; Talegawkar, S. A.; et al. The World Health Organization Fetal Growth Charts: A Multinational Longitudinal Study of Ultrasound Biometric Measurements and Estimated Fetal Weight. *PLoS Med.* **2017**, *14* (1), 1002220.
- (2) Blomley, M. J. K.; Cooke, J. C.; Unger, E. C.; Monaghan, M. J.; Cosgrove, D. O. Science, Medicine, and the Future: Microbubble Contrast Agents: A New Era in Ultrasound. *Br. Med. J.* **2001**, *322* (7296), 1222–1225.
- (3) Kelly, S. P.; Farlow, R.; Hayward, G. Applications of Through-Air Ultrasound for Rapid NDE Scanning in the Aerospace Industry. *IEEE Trans. Ultrason. Ferroelectr. Freq. Control* **1996**, *43* (4), 581–591.
- (4) Turantaş, F.; Kiliç, G. B.; Kiliç, B. Ultrasound in the Meat Industry: General Applications and Decontamination Efficiency. *Int. J. Food Microbiol.* **2015**, *198*, 59–69.
- (5) Roberts, W. W.; Hall, T. L.; Ives, K.; Wolf, J. S.; Fowlkes, J. B.; Cain, C. A. Pulsed Cavitation Ultrasound: A Noninvasive Technology for Controlled Tissue Ablation (Histotripsy) in the Rabbit Kidney. *J. Urol.* **2006**, *175* (2), 734–738.
- (6) Sikdar, S.; Shah, J. P.; Gebreab, T.; Yen, R. H.; Gilliams, E.; Danoff, J.; Gerber, L. H. Novel Applications of Ultrasound Technology to Visualize and Characterize Myofascial Trigger Points and Surrounding Soft Tissue. *Arch. Phys. Med. Rehabil.* **2009**, *90* (11), 1829–1838.
- (7) Kruger, R. A.; Liu, P.; Fang, Y. R.; Appledorn, C. R. Photoacoustic Ultrasound (PAUS)—Reconstruction Tomography. *Med. Phys.* **1995**, *22* (10), 1605–1609.
- (8) Xu, M.; Wang, L. V. Photoacoustic Imaging in Biomedicine. *Rev. Sci. Instrum.* **2006**, *77* (4).

- (9) Kircher, M. F.; De La Zerda, A.; Jokerst, J. V.; Zavaleta, C. L.; Kempen, P. J.; Mittra, E.; Pitter, K.; Huang, R.; Campos, C.; Habte, F.; et al. A Brain Tumor Molecular Imaging Strategy Using a New Triple-Modality MRI-Photoacoustic-Raman Nanoparticle. *Nat. Med.* **2012**, *18* (5), 829–834.
- (10) Tam, A. C. Applications of Photoacoustic Sensing Techniques. *Rev. Mod. Phys.* **1986**, *58* (2), 381–431.
- (11) Shinoda, H.; Nakajima, T.; Ueno, K.; Koshida, N. Thermally Induced Ultrasonic Emission from Porous Silicon. *Nature* **1999**, *400* (6747), 853–855.
- (12) Dutta, R.; Albee, B.; Van Der Veer, W. E.; Harville, T.; Donovan, K. C.; Papamoschou, D.; Penner, R. M. Gold Nanowire Thermophones. *J. Phys. Chem. C* **2014**, *118* (50), 29101–29107.
- (13) Tian, H.; Xie, D.; Yang, Y.; Ren, T. L.; Feng, T. T.; Wang, Y. F.; Zhou, C. J.; Peng, P. G.; Wang, L. G.; Liu, L. T. Poly(3,4-Ethylenedioxythiophene):Poly(Styrenesulfonate)-Based Organic, Ultrathin, and Transparent Sound-Emitting Device. *Appl. Phys. Lett.* **2011**, *99* (23), 253507.
- (14) Tian, H.; Xie, D.; Yang, Y.; Ren, T. L.; Lin, Y. X.; Chen, Y.; Wang, Y. F.; Zhou, C. J.; Peng, P. G.; Wang, L. G.; et al. Flexible, Ultrathin, and Transparent Sound-Emitting Devices Using Silver Nanowires Film. *Appl. Phys. Lett.* **2011**, *99* (25), 253507.
- (15) Tian, H.; Xie, D.; Yang, Y.; Ren, T. L.; Wang, Y. F.; Zhou, C. J.; Peng, P. G.; Wang, L. G.; Liu, L. T. Transparent, Flexible, Ultrathin Sound Source Devices Using Indium Tin Oxide Films. *Appl. Phys. Lett.* **2011**, *99* (4), 043503.
- (16) Daschewski, M.; Boehm, R.; Prager, J.; Kreuzbruck, M.; Harrer, A. Physics of Thermo-Acoustic Sound Generation. *J. Appl. Phys.* **2013**, *114* (11), 114903.
- (17) Tian, H.; Ren, T. L.; Xie, D.; Wang, Y. F.; Zhou, C. J.; Feng, T. T.; Fu, D.; Yang, Y.; Peng, P. G.; Wang, L. G.; et al. Graphene-on-Paper Sound Source Devices. *ACS*

Nano **2011**, 5 (6), 4878–4885.

- (18) Xiao, L.; Liu, P.; Liu, L.; Li, Q.; Feng, Z.; Fan, S.; Jiang, K. High Frequency Response of Carbon Nanotube Thin Film Speaker in Gases. *J. Appl. Phys.* **2011**, 110 (8), 084311.
- (19) Vesterinen, V.; Niskanen, A. O.; Hassel, J.; Helistö, P. Fundamental Efficiency of Nanothermophones: Modeling and Experiments. *Nano Lett.* **2010**, 10 (12), 5020–5024.
- (20) Iijima, S.; Ichihashi, T. Single-Shell Carbon Nanotubes of 1-Nm Diameter. *Nature* **1993**, 363 (6430), 603–605.
- (21) Iijima, S. Helical Microtubules of Graphitic Carbon. *Nature* **1991**, 354 (6348), 56–58.
- (22) Baughman, R. H.; Zakhidov, A. A.; De Heer, W. A. Carbon Nanotubes - The Route toward Applications. *Science (80-.)*. **2002**, 297 (5582), 787–792.
- (23) De Volder, M. F. L.; Tawfick, S. H.; Baughman, R. H.; Hart, A. J. Carbon Nanotubes: Present and Future Commercial Applications. *Science (80-.)*. **2013**, 339 (6119), 535–539.
- (24) Yu, L.; Shearer, C.; Shapter, J. Recent Development of Carbon Nanotube Transparent Conductive Films. *Chem. Rev.* **2016**, 116 (22), 13413–13453.
- (25) Timmermans, M. Y.; Estrada, D.; Nasibulin, A. G.; Wood, J. D.; Behnam, A.; Sun, D. ming; Ohno, Y.; Lyding, J. W.; Hassanien, A.; Pop, E.; et al. Effect of Carbon Nanotube Network Morphology on Thin Film Transistor Performance. *Nano Res.* **2012**, 5 (5), 307–319.
- (26) Rajanna, P. M.; Meddeb, H.; Sergeev, O.; Tsapenko, A. P.; Bereznev, S.; Vehse, M.; Volobujeva, O.; Danilson, M.; Lund, P. D.; Nasibulin, A. G. Rational Design of Highly Efficient Flexible and Transparent P-Type Composite Electrode Based on Single-Walled Carbon Nanotubes. *Nano Energy* **2020**, 67, 104183.

- (27) Accredited Standards Committee S1, A. American National Standard: Acoustical Terminology. ANSI/ASA S1.1-2013. *Ansi S1.1-1994* **2014**, 2013, 58.
- (28) Carovac, A.; Smajlovic, F.; Junuzovic, D. Application of Ultrasound in Medicine. *Acta Inform. Medica* **2011**, 19 (3), 168.
- (29) Chemat, F.; Rombaut, N.; Sicaire, A. G.; Meullemiestre, A.; Fabiano-Tixier, A. S.; Abert-Vian, M. Ultrasound Assisted Extraction of Food and Natural Products. Mechanisms, Techniques, Combinations, Protocols and Applications. A Review. *Ultrason. Sonochem.* **2017**, 34, 540–560.
- (30) Bang, J. H.; Suslick, K. S. Applications of Ultrasound to the Synthesis of Nanostructured Materials. *Adv. Mater.* **2010**, 22 (10), 1039–1059.
- (31) Wang, X.; Song, J.; Liu, J.; Zhong, L. W. Direct-Current Nanogenerator Driven by Ultrasonic Waves. *Science (80-.)*. **2007**, 316 (5821), 102–105.
- (32) Johnson, J. B.; Ripepe, M. Volcano Infrasound: A Review. *J. Volcanol. Geotherm. Res.* **2011**, 206 (3–4), 61–69.
- (33) Beard, P. Biomedical Photoacoustic Imaging. *Interface Focus* **2011**, 1 (4), 602–631.
- (34) Cosgrove, D. Ultrasound Contrast Agents: An Overview. *Eur. J. Radiol.* **2006**, 60 (3), 324–330.
- (35) Farmer, A. D.; Collings, A. F.; Jameson, G. J. Effect of Ultrasound on Surface Cleaning of Silica Particles. *Int. J. Miner. Process.* **2000**, 60 (2), 101–113.
- (36) Hawkes, J. J.; Barber, R. W.; Emerson, D. R.; Coakley, W. T. Continuous Cell Washing and Mixing Driven by an Ultrasound Standing Wave within a Microfluidic Channel. *Lab Chip* **2004**, 4 (5), 446–452.
- (37) Ter Haar, G. Ultrasound Focal Beam Surgery. *Ultrasound Med. Biol.* **1995**, 21 (9), 1089–1100.
- (38) Suslick, K. S. Sonochemistry. *Science (80-.)*. **1990**, 247 (4949), 1439–1445.

- (39) Fenster, A.; Downey, D. B.; Cardinal, H. N. Three-Dimensional Ultrasound Imaging. *Phys. Med. Biol.* **2001**, *46* (5).
- (40) Kennedy, J. E. High-Intensity Focused Ultrasound in the Treatment of Solid Tumours. *Nat. Rev. Cancer* **2005**, *5* (4), 321–327.
- (41) Balle, F.; Wagner, G.; Eifler, D. Ultrasonic Metal Welding of Aluminium Sheets to Carbon Fibre Reinforced Thermoplastic Composites. *Adv. Eng. Mater.* **2009**, *11* (1–2), 35–39.
- (42) Persinger, M. A. Infrasound, Human Health, and Adaptation: An Integrative Overview of Recondite Hazards in a Complex Environment. *Nat. Hazards* **2014**, *70* (1), 501–525.
- (43) Mutschlecner, J. P.; Whitaker, R. W. Infrasound from Earthquakes. *J. Geophys. Res. D Atmos.* **2005**, *110* (1), 1–11.
- (44) Fee, D.; Matoza, R. S. An Overview of Volcano Infrasound: From Hawaiian to Plinian, Local to Global. *J. Volcanol. Geotherm. Res.* **2013**, *249*, 123–139.
- (45) Drob, D. P.; Picone, J. M.; Garcés, M. Global Morphology of Infrasound Propagation. *J. Geophys. Res. Atmos.* **2003**, *108* (21).
- (46) Bowman, H. S.; Bedard, A. J. Observations of Infrasound and Subsonic Disturbances Related to Severe Weather. *Geophys. J. R. Astron. Soc.* **1971**, *26* (1–4), 215–242.
- (47) Le Pichon, A.; Blanc, E.; Hauchecorne, A. Infrasound Monitoring for Atmospheric Studies: Challenges in Middle Atmosphere Dynamics and Societal Benefits: Second Edition. *Infrasound Monit. Atmos. Stud. Challenges Middle Atmos. Dyn. Soc. Benefits Second Ed.* **2018**, 1–1167.
- (48) Persbo, A. Compliance Science: The CTBT’s Global Verification System. *Nonproliferation Rev.* **2016**, *23* (3–4), 317–328.

- (49) Rijke, P. L. LXXI. Notice of a New Method of Causing a Vibration of the Air Contained in a Tube Open at Both Ends . *London, Edinburgh, Dublin Philos. Mag. J. Sci.* **1859**, *17* (116), 419–422.
- (50) Backhaus, S.; Swift, G. W. A Thermoacoustic Stirling Heat Engine. *Nature* **1999**, *399* (6734), 335–338.
- (51) Wollan, J. J.; Swift, G. W.; Backhaus, S.; Gardner, D. L. Development of Thermoacoustic Natural Gas Liquefier. *Proc. AIChE Meet.* **2002**, 1–8.
- (52) Backhaus, S.; Swift, G. New Varieties of Thermoacoustic Engines. *Ninth Int. Congr. Sound Vib.* **2002**, 1–8.
- (53) Loh, A.; Keen, W.; Rilling, D. Feasibility Study of Thermoacoustic Lamina Flow Engine for Waste Heat Regeneration in Vehicles 2 Availability of Waste Heat 3 Lamina Flow Engine. *Wseas Conf.* **2010**, 84–88.
- (54) Zoontjens, L.; Howard, C.; Zander, A.; Cazzolato, B. Feasibility Study of an Automotive Thermoacoustic Refrigerator. *Annu. Conf. Aust. Acoust. Soc. 2005, Acoust. 2005 Acoust. a Chang. Environ.* **2005**, 299–307.
- (55) Symko, O. G.; Abdel-Rahman, E.; Kwon, Y. S.; Emmi, M.; Behunin, R. Design and Development of High-Frequency Thermoacoustic Engines for Thermal Management in Microelectronics. *Microelectronics J.* **2004**, *35* (2), 185–191.
- (56) Chen, K.; Oh, S. J.; Lee, Y. J.; Oh, W. J.; Kim, K. H.; Chun, W. Acoustic Energy Output and Coupling Effect of a Pair of Thermoacoustic Lasers. *Int. J. Energy Res.* **2012**, *36* (4), 477–485.
- (57) Tijani, H.; Spoelstra, S.; Lycklama, J. A. High Temperature Thermoacoustic Heat Pump. *19th Int. Congr. Sound Vib. 2012, ICSV 2012* **2012**, *4*, 2559–2565.
- (58) Bell, A. G. LXVIII. Upon the Production of Sound by Radiant Energy . *London, Edinburgh, Dublin Philos. Mag. J. Sci.* **1881**, *11* (71), 510–528.

- (59) Sigrist, M. W. Trace Gas Monitoring by Laser Photoacoustic Spectroscopy and Related Techniques (Plenary). *Rev. Sci. Instrum.* **2003**, *74* (1 II), 486–490.
- (60) Fischer, C.; Sorokin, E.; Sorokina, I. T.; Sigrist, M. W. Photoacoustic Monitoring of Gases Using a Novel Laser Source Tunable around 2.5 Mm. *Opt. Lasers Eng.* **2005**, *43* (3–5), 573–582.
- (61) Rosencwaig, A.; Gersho, A. Theory of the Photoacoustic Effect with Solids. *J. Appl. Phys.* **1976**, *47* (1), 64–69.
- (62) Braun, F. Notiz Über Thermophonie. *Ann. Phys.* **1898**, *301.6*, 358–360.
- (63) Arnold, H. D.; Crandall, I. B. The Thermophone as a Precision Source of Sound. *Phys. Rev.* **1917**, *10* (1), 22–38.
- (64) Xiao, L.; Chen, Z.; Feng, C.; Liu, L.; Bai, Z. Q.; Wang, Y.; Qian, L.; Zhang, Y.; Li, Q.; Jiang, K.; et al. Flexible, Stretchable, Transparent Carbon Nanotube Thin Film Loudspeakers. *Nano Lett.* **2008**, *8* (12), 4539–4545.
- (65) Yang, F.; Wang, M.; Zhang, D.; Yang, J.; Zheng, M.; Li, Y. Chirality Pure Carbon Nanotubes: Growth, Sorting, and Characterization. *Chem. Rev.* **2020**, *120* (5), 2693–2758.
- (66) Mubarak, N. M.; Abdullah, E. C.; Jayakumar, N. S.; Sahu, J. N. An Overview on Methods for the Production of Carbon Nanotubes. *J. Ind. Eng. Chem.* **2014**, *20* (4), 1186–1197.
- (67) Nasibulin, A. G.; Moisala, A.; Brown, D. P.; Jiang, H.; Kauppinen, E. I. A Novel Aerosol Method for Single Walled Carbon Nanotube Synthesis. *Chem. Phys. Lett.* **2005**, *402* (1–3), 227–232.
- (68) Moisala, A.; Nasibulin, A. G.; Brown, D. P.; Jiang, H.; Khriachtchev, L.; Kauppinen, E. I. Single-Walled Carbon Nanotube Synthesis Using Ferrocene and Iron Pentacarbonyl in a Laminar Flow Reactor. *Chem. Eng. Sci.* **2006**, *61* (13), 4393–4402.

- (69) Kaskela, A.; Nasibulin, A. G.; Timmermans, M. Y.; Aitchison, B.; Papadimitratos, A.; Tian, Y.; Zhu, Z.; Jiang, H.; Brown, D. P.; Zakhidov, A.; et al. Aerosol-Synthesized SWCNT Networks with Tunable Conductivity and Transparency by a Dry Transfer Technique. *Nano Lett.* **2010**, *10* (11), 4349–4355.
- (70) Nasibulin, A. G.; Kaskela, A.; Mustonen, K.; Anisimov, A. S.; Ruiz, V.; Kivistö, S.; Rackauskas, S.; Timmermans, M. Y.; Pudas, M.; Aitchison, B.; et al. Multifunctional Free-Standing Single-Walled Carbon Nanotube Films. *ACS Nano* **2011**, *5* (4), 3214–3221.
- (71) Anisimov, A. S.; Nasibulin, A. G.; Jiang, H.; Launois, P.; Cambedouzou, J.; Shandakov, S. D.; Kauppinen, E. I. Mechanistic Investigations of Single-Walled Carbon Nanotube Synthesis by Ferrocene Vapor Decomposition in Carbon Monoxide. *Carbon N. Y.* **2010**, *48* (2), 380–388.
- (72) Wang, Z. L. New Developments in Transmission Electron Microscopy for Nanotechnology. *Adv. Mater.* **2003**, *15* (18), 1497–1514.
- (73) Urban, K. W. Studying Atomic Structures by Aberration-Corrected Transmission Electron Microscopy. *Science (80-.)*. **2008**, *321* (5888), 506–510.
- (74) Bauer, E. Surface Electron Microscopy: The First Thirty Years. *Surf. Sci.* **1994**, *299–300* (C), 102–115.
- (75) Stokes, D. J. Recent Advances in Electron Imaging, Image Interpretation and Applications: Environmental Scanning Electron Microscopy. *Philos. Trans. R. Soc. A Math. Phys. Eng. Sci.* **2003**, *361* (1813), 2771–2787.
- (76) Dens Solution <https://denssolutions.com/>.
- (77) Hazle, M. A.; Mehicic, M.; Gardiner, D. J.; Graves, P. R. Practical Raman Spectroscopy. *Vib. Spectrosc.* **1990**, *1* (1), 104.
- (78) Dresselhaus, M. S.; Dresselhaus, G.; Saito, R.; Jorio, A. Raman Spectroscopy of Carbon Nanotubes. *Phys. Rep.* **2005**, *409* (2), 47–99.

- (79) Kataura, H.; Kumazawa, Y.; Maniwa, Y.; Umezu, I.; Suzuki, S.; Ohtsuka, Y.; Achiba, Y. Optical Properties of Single-Wall Carbon Nanotubes. *Synth. Met.* **1999**, *103* (1–3), 2555–2558.
- (80) Milnera, M.; Rouse, R.; Rouse, R. Periodic Resonance Excitation and Intertube Interaction from Quasicontinuous Distributed Helicities in Single-Wall Carbon Nanotubes. *Phys. Rev. Lett.* **2000**, *84* (6), 1324–1327.
- (81) Dresselhaus, M. S.; Jorio, A.; Hofmann, M.; Dresselhaus, G.; Saito, R. Perspectives on Carbon Nanotubes and Graphene Raman Spectroscopy. *Nano Lett.* **2010**, *10* (3), 751–758.
- (82) Chabal, Y. J. Surface Infrared Spectroscopy. *Surf. Sci. Rep.* **1988**, *8* (5–7), 211–357.
- (83) Berthomieu, C.; Hienerwadel, R. Fourier Transform Infrared (FTIR) Spectroscopy. *Photosynth. Res.* **2009**, *101* (2–3), 157–170.
- (84) Țucureanu, V.; Matei, A.; Avram, A. M. FTIR Spectroscopy for Carbon Family Study. *Crit. Rev. Anal. Chem.* **2016**, *46* (6), 502–520.
- (85) Aliev, A. E.; Gartstein, Y. N.; Baughman, R. H. Increasing the Efficiency of Thermoacoustic Carbon Nanotube Sound Projectors. *Nanotechnology* **2013**, *24* (23).
- (86) Pierce, A. D. Acoustics: An Introduction to Its Physical Principles and Applications. *Springer* **2019**.
- (87) Sapozhnikov, O. A. High-Intensity Ultrasonic Waves in Fluids: Nonlinear Propagation and Effects. *Power Ultrason. Appl. High-Intensity Ultrasound* **2015**, 9–35.
- (88) Gusev, V. E.; Karabutov, A. A. Laser Optoacoustics_Vitaly Gusev.Pdf. *Stia* **1993**, *93*, 16842.
- (89) Rohsenow, W. M.; Hartnett, J. R. Handbook of Heat Transfer, 3rd Edition. *Choice*

Rev. Online **1999**, 1501.

- (90) Vinet, L.; Zhedanov, A. A “missing” Family of Classical Orthogonal Polynomials. *J. Phys. A Math. Theor.* **2011**, *44* (8).
- (91) Ma, Y.; He, Z.; Peng, X.; Xing, Z. Experimental Investigation of the Discharge Valve Dynamics in a Reciprocating Compressor for Trans-Critical CO₂ Refrigeration Cycle. *Appl. Therm. Eng.* **2012**, *32* (1), 13–21.
- (92) Moscardini, M.; Gan, Y.; Pupleschi, S.; Kamlah, M. Discrete Element Method for Effective Thermal Conductivity of Packed Pebbles Accounting for the Smoluchowski Effect. *Fusion Eng. Des.* **2018**, *127*, 192–201.
- (93) Xiao, B.; Dong, T.; Halvorsen, E.; Yang, Z.; Zhang, Y.; Hoivik, N.; Gu, D.; Tran, N. M.; Jakobsen, H. Integrated Micro Pirani Gauge Based Hermetical Package Monitoring for Uncooled VO_x Bolometer FPAs. *Microsyst. Technol.* **2011**, *17* (1), 115–125.
- (94) Churchill, S. W.; Chu, H. H. S. Correlating Equations for Laminar and Turbulent Free Convection from a Vertical Plate. *Int. J. Heat Mass Transf.* **1975**, *18* (11), 1323–1329.
- (95) Kumanek, B.; Janas, D. Thermal Conductivity of Carbon Nanotube Networks: A Review. *J. Mater. Sci.* **2019**, *54* (10), 7397–7427.
- (96) Romanov, S. A.; Aliev, A. E.; Fine, B. V.; Anisimov, A. S.; Nasibulin, A. G. Highly Efficient Thermophones Based on Freestanding Single-Walled Carbon Nanotube Films. *Nanoscale Horizons* **2019**, *4* (5), 1158–1163.
- (97) Zhang, M.; Fang, S.; Zakhidov, A. A.; Lee, S. B.; Aliev, A. E.; Williams, C. D.; Atkinson, K. R.; Baughman, R. H. Materials Science: Strong, Transparent, Multifunctional, Carbon Nanotube Sheets. *Science (80-.)*. **2005**, *309* (5738), 1215–1219.
- (98) Barnard, A. R.; Jenkins, D. M.; Brungart, T. A.; McDevitt, T. M.; Kline, B. L.

Feasibility of a High-Powered Carbon Nanotube Thin-Film Loudspeaker. *J. Acoust. Soc. Am.* **2013**, *134* (3), EL276-EL281.

- (99) Andrews, R.; Jacques, D.; Qian, D.; Dickey, E. C. Purification and Structural Annealing of Multiwalled Carbon Nanotubes at Graphitization Temperatures. *Carbon N. Y.* **2001**, *39* (11), 1681–1687.
- (100) Kim, Y. A.; Hayashi, T.; Osawa, K.; Dresselhaus, M. S.; Endo, M. Annealing Effect on Disordered Multi-Wall Carbon Nanotubes. *Chem. Phys. Lett.* **2003**, *380* (3–4), 319–324.
- (101) Huang, W.; Wang, Y.; Luo, G.; Wei, F. 99.9% Purity Multi-Walled Carbon Nanotubes By Vacuum High-Temperature Annealing. *Carbon N. Y.* **2003**, *41* (13), 2585–2590.
- (102) Kulkarni, P.; Baron, P. A.; Willeke, K. Aerosol Measurement: Principles, Techniques, and Applications: Third Edition. *Aerosol Meas. Princ. Tech. Appl. Third Ed.* **2011**.
- (103) Romanov, S. A. In situ iron evaporation in TEM <https://youtu.be/tw-1mC78beA>.
- (104) Shandakov, S. D.; Lomakin, M. V.; Nasibulin, A. G. The Effect of the Environment on the Electronic Properties of Single-Walled Carbon Nanotubes. *Tech. Phys. Lett.* **2016**, *42* (11), 1071–1075.
- (105) Kim, S.; Kim, H. J.; Lee, H. R.; Song, J. H.; Yi, S. N.; Ha, D. H. Oxygen Plasma Effects on the Electrical Conductance of Single-Walled Carbon Nanotube Bundles. *J. Phys. D. Appl. Phys.* **2010**, *43* (30), 305402.
- (106) Grigoras, K.; Zavodchikova, M. Y.; Nasibulin, A. G.; Kauppinen, E. I.; Ermolov, V.; Franssilal, S. Atomic Layer Deposition of Aluminum Oxide Films for Carbon Nanotube Network Transistor Passivation. *J. Nanosci. Nanotechnol.* **2011**, *11* (10), 8818–8825.
- (107) Aliev, A. E.; Codoluto, D.; Baughman, R. H.; Ovalle-Robles, R.; Inoue, K.;

- Romanov, S. A.; Nasibulin, A. G.; Kumar, P.; Priya, S.; Mayo, N. K.; et al. Thermoacoustic Sound Projector: Exceeding the Fundamental Efficiency of Carbon Nanotubes. *Nanotechnology* **2018**, *29* (32).
- (108) Aliev, A. E.; Mayo, N. K.; Baughman, R. H.; Avirovik, D.; Priya, S.; Zarnetske, M. R.; Blottman, J. B. Thermoacoustic Excitation of Sonar Projector Plates by Free-Standing Carbon Nanotube Sheets. *J. Phys. D. Appl. Phys.* **2014**, *47* (35), 355302.
- (109) Office, U. states patent and trademark. <https://www.uspto.gov/>.
- (110) Filonenko, V.; Cullen, C.; Carswell, J. D. Indoor Positioning for Smartphones Using Asynchronous Ultrasound Trilateration. *ISPRS Int. J. Geo-Information* **2013**, *2* (3), 598–620.
- (111) Medina, C.; Segura, J. C.; De la Torre, Á. Ultrasound Indoor Positioning System Based on a Low-Power Wireless Sensor Network Providing Sub-Centimeter Accuracy. *Sensors (Switzerland)* **2013**, *13* (3), 3501–3526.
- (112) Hazas, M.; Hopper, A. Broadband Ultrasonic Location Systems for Improved Indoor Positioning. *IEEE Trans. Mob. Comput.* **2006**, *5* (5), 536–547.

Appendix: List of variables

α is the thermal expansion coefficient

$\alpha(\lambda)$ is the absorption coefficient dependence on the wavelength

α_T is the thermal diffusivity

β is the compressibility

β_t is the amount of energy transfer between the gas molecule and the solid material

γ_f is the surface tension

γ is the heat capacity ratio of air

δp is the increment of pressure

δT is the increment of temperature

ξ is the film optical transmittance

η is the absolute efficiency of the thermophones

η_{lim} is the absolute efficiency of the thermophones in the ultimate limit

θ is the polar angles

κ is the thermal conductivity of air

λ is a molecule mean free path

λ is the sound wavelength

λ is the light wavelength

μ is a dynamic viscosity of air

ρ is the density

ρ_a is the areal density of the sample

ρ_h is the sample density

ρ_g is the air density

ρ_p is the density of an iron particle

φ is the azimuth angle

ω is the angular frequency

A is the temperature oscillation amplitude inside a volumetric heater

B is the temperature oscillation amplitude outside a volumetric heater

C_i is the empirical constant

C_h is the heat capacity of heating material per unit mass (specific heat capacity)

C_s is the heat capacity per unit area

C_g is the heat capacity of air per unit mass (specific heat capacity)

C_p is a specific heat capacity of fluid at a constant pressure.

C_V is heat capacity per unit volume

D is the directivity of a square sound emitter

D_s is the signal duty cycle

I is the sound intensity

I_G is the intensity of G mode in Raman spectrum

I_D is the intensity of D mode in Raman spectrum

G is the intensity gain function

Kn is the Knudsen number

L is the wall length

M is the iron molar mass.

P_0 is the time averaged electrical input power

P_a is the average acoustic power

P_{conv} is the power dissipated because of the convection effect

P_{cond} is the power dissipated because of the conduction effect

P_{rad} is the power dissipated because of the radiation effect

P_{el} is the input electrical power

P is the gas pressure

P_m partial vapor pressures of iron within the media

P_p partial vapor pressures of iron over the particle

P_∞ is the equilibrium vapor pressure for the bulk

Q is a volumetric heat density

R is the universal gas constant

Ra is a Rayleigh number

S is the surface area,

T_{avg} is the amplitude of the sample average temperature

T_{osc} is the amplitude of periodic temperature oscillations

T_1 amplitudes of temperatures oscillations inside of the volumetric heater

T_2 amplitudes of temperatures oscillations outside of the volumetric heater

T is the sample temperature

T_0 is the temperature of surrounding media

V is the sample volume

V_m is the molar volume

a_c is the thermal accommodation coefficient,

a_0 is an attenuation coefficient

a is the sphere radius

c is the speed of light

d is the size of the confined space

d_m is the kinetic diameter of gas molecule

h is the thickness of the sample

h_{conv} the heat transfer coefficient from the film

k is the sound wavenumber

k_B is the Boltzmann constant,

k_{air} is the thermal conductivity of air at ambient pressure

k_{vac} is the thermal conductivity of vacuum

l is the thermal diffusion length

m_r is the ratio of the gas to solid atomic masses

p is the sound pressure

p_{rms} is the root mean square of the sound pressure

q is the thermal wave number

q_1 is the thermal wave number inside a volumetric heater

q_2 is the thermal wave number outside a volumetric heater

r is the radius

t is the time

t_h is the heating time

t_c is the cooling time

u is the velocity field

v_s is the speed of sound

x is the axis of the coordinate